The Astrophysical Journal, 838:122 (20pp), 2017 April 1 https://doi.org/10.3847/1538-4357/aa65cb

General Model for Light Curves of Chromospherically Active Binary Stars*

L. Jetsu[1], G. W. Henry[2], and J. Lehtinen[3]
[1] Department of Physics, FI-00014 University of Helsinki, Finland; lauri.jetsu@helsinki.fi
[2] Center of Excellence in Information Systems, Tennessee State University, Nashville, TN 37209, USA
[3] Max-Planck-Institut für Sonnensystemforschung, D-37077 Göttingen, Germany
Received 2016 December 6; revised 2017 February 20; accepted 2017 March 5; published 2017 March 31

Abstract

The starspots on the surface of many chromospherically active binary stars concentrate on long-lived active longitudes separated by 180°. Shifts in activity between these two longitudes, the "flip-flop" events, have been observed in single stars like FK Comae and binary stars like σ Geminorum. Recently, interferometry has revealed that ellipticity may at least partly explain the flip-flop events in σ Geminorum. This idea was supported by the double-peaked shape of the long-term mean light curve of this star. Here we show that the long-term mean light curves of 14 chromospherically active binaries follow a general model that explains the connection between orbital motion, changes in starspot distribution, ellipticity, and flip-flop events. Surface differential rotation is probably weak in these stars, because the interference of two constant period waves may explain the observed light curve changes. These two constant periods are the active longitude period ($P_{\rm act}$) and the orbital period ($P_{\rm orb}$). We also show how to apply the same model to single stars, where only the value of $P_{\rm act}$ is known. Finally, we present a tentative interference hypothesis about the origin of magnetic fields in all spectral types of stars.

Key words: binaries: general – methods: data analysis – stars: activity – techniques: photometric

Supporting material: data behind figures

1. Introduction

An ancient Egyptian calendar of lucky and unlucky days, the Cairo Calendar, is the oldest preserved historical document of the discovery of a variable star, Algol (Porceddu et al. 2008; Jetsu et al. 2013; Jetsu & Porceddu 2015). Today, the General Catalogue of Variable Stars contains nearly 50,000 stars. There are numerous classes of variable stars, and the classification criteria are constantly updated (Samus et al. 1997). Different classes have their own typical light curves (Drake et al. 2014). One class of variable stars is called the Chromospherically Active Binary Stars (hereafter CABS). The third CABS catalogue lists 409 such binaries (Eker et al. 2008).

In his review of starspots, Strassmeier (2009) wrote that the "starspot hypothesis" was first presented by the French astronomer Ismael Boulliau (1605–1694) to explain the variability of Mira. This star, also known as *o* Ceti, was the first variable star discovered by "modern" astronomers in 1596 (David Fabricius, 1564–1617). Boulliau's hypothesis was unfortunately not true, because pulsations cause the variability of Mira. According to Strassmeier (2009), the first observations of starspots were made by Kron (1947) in the light curves of four eclipsing binaries. The presence of this phenomenon in the light curves of active stars was firmly established later by Hoffmeister (1965), Chugainov (1966), Catalano & Rodonò (1967), and Hall (1972).

Unlike the longitudinally uniform distribution of spots on the Sun, the starspots in active single (e.g., Jetsu et al. 1993, FK Com) or binary (e.g., Jetsu 1996, σ Gem) stars concentrate at long-lived active longitudes and seem to undergo shifts of about 180° in longitude. The presence of this "flip-flop" phenomenon in the CABS σ Gem was questioned by Roettenbacher et al. (2015). Their interferometric observations revealed that ellipticity of σ Gem may explain the stability of the two minima in the long-term mean light curve (hereafter MLC). Recently, Siltala et al. (2016) reported that another CABS, BM CVn, has a sinusoidal MLC with an amplitude of $0\overset{\rm m}{.}042$. Ellipticity fails to explain the MLC shape of BM CVn. Here we study the light curves of fourteen CABS. Our sample includes the light curves of the two previously mentioned CABS, σ Gem and BM CVn.

We use the following abbreviations:

CABS = Chromospherically active binary star
MLC = Mean light curve
CPS = Continuous period search
A = More active CABS component
B = Other CABS component
Aa = A in front of B epoch at $\phi_{\rm orb} = 0.75$
Ac = B in front of A epoch at $\phi_{\rm orb} = 0.25$
Ab = Mid epoch between Aa and Ac at $\phi_{\rm orb} = 0.00$
Ad = Mid epoch between Ac and Aa at $\phi_{\rm orb} = 0.50$
S1 = Larger stationary starspot on A
S2 = Smaller stationary starspot on A
S1f = S1 visibility maximum at Aa and No S2
S1b = S1 visibility maximum at Ac and No S2
S12fb = S1 visibility maximum and S2 unseen at Aa
S12bf = S1 unseen and S2 visibility maximum at Aa
S3 = Larger nonstationary starspot on A
S4 = Smaller nonstationary starspot on A.

The meaning of the last 12 abbreviations is explained in greater detail in Section 6. We emphasize that the previously listed Aa, Ab, Ac, and Ad epochs are used to connect the results in Figures 1–27 unambiguously to the sketches of Figures 28 and 29.

2. Observations

We have acquired between 23 and 27 years of time series differential *V* photometric observations of 14 chromospherically

* The CPS results are available electronically at the Vizier database.

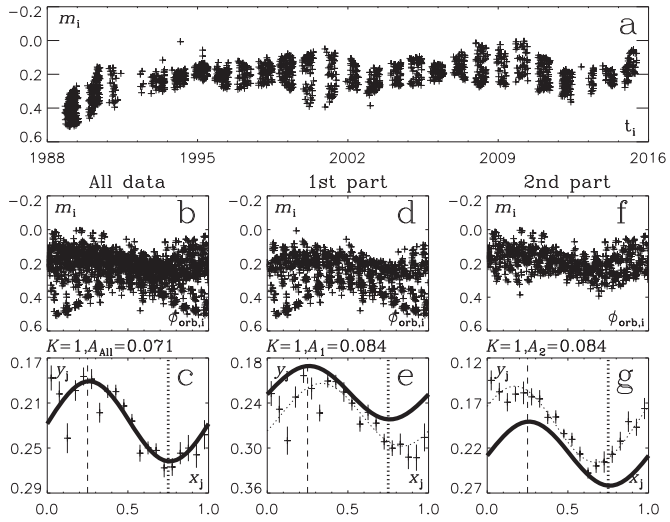

Figure 1. DM UMa. (a) All data: V magnitudes (crosses) vs. time. (b) All data: V magnitudes (crosses) vs. orbital phase. (c) All data: binned magnitudes (crosses with error bars), MLC (thick continuous line), order (K), and amplitude ($A_{\rm All}$). Epoch Aa (thick dotted vertical line) and epoch Ac (thin dashed vertical line). (d) First part of data: V magnitudes (crosses) vs. orbital phase. (e) First part of data: binned magnitudes (crosses with error bars), MLC (thin dashed line), order (K), amplitude (A_1), and MLC of all data (thick line from "a"). Epoch Aa (thick dotted vertical line) and epoch Ac (thin dashed vertical line). (f and g) Second part of data: otherwise as in panels d and e. (The data used to create this figure are available.)

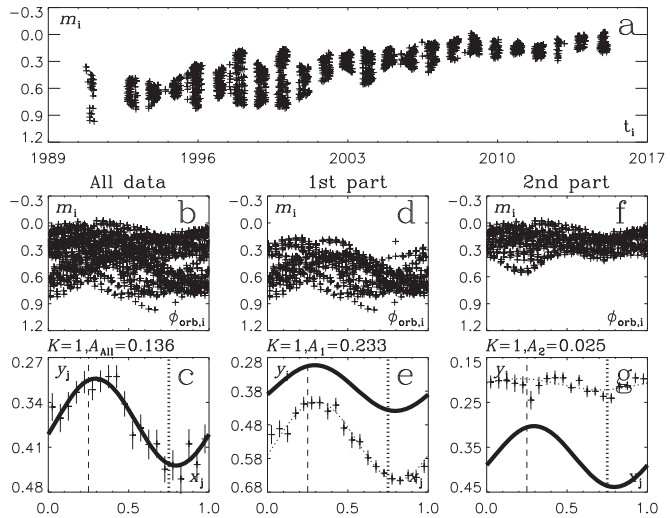

Figure 2. XX Tri. Notice the dips in (g) at $\phi_{\rm orb} \approx 0.25$ and 0.75; otherwise as in Figure 1.
(The data used to create this figure are available.)

active binaries with Tennessee State University's T3 0.4 m automatic photometric telescope located at Fairborn Observatory in southern Arizona. The precision of the individual photometric measurements averages around $0^{\rm m}.005$ on good photometric nights (see Henry et al. 1995b, Table 3). A summary of the photometric observations is given in Table 1.

3. MLC Analysis

The $P_{\rm orb}$ and t_0 values of each CABS (Eker et al. 2008) are given in Table 1. There are five different types of radial

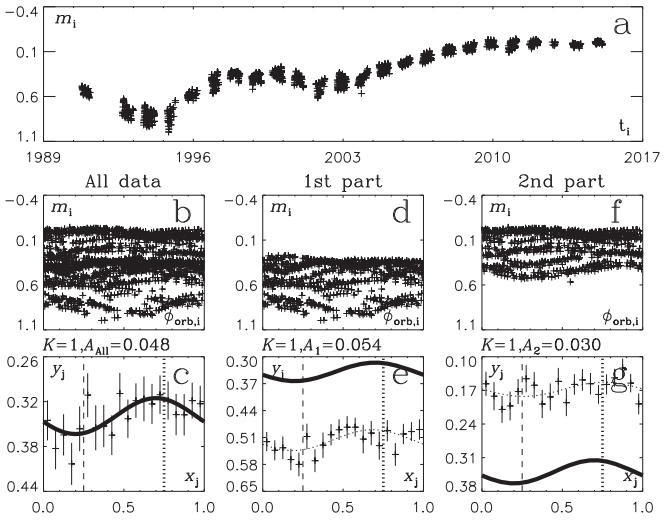

Figure 3. EL Eri, otherwise as in Figure 1.
(The data used to create this figure are available.)

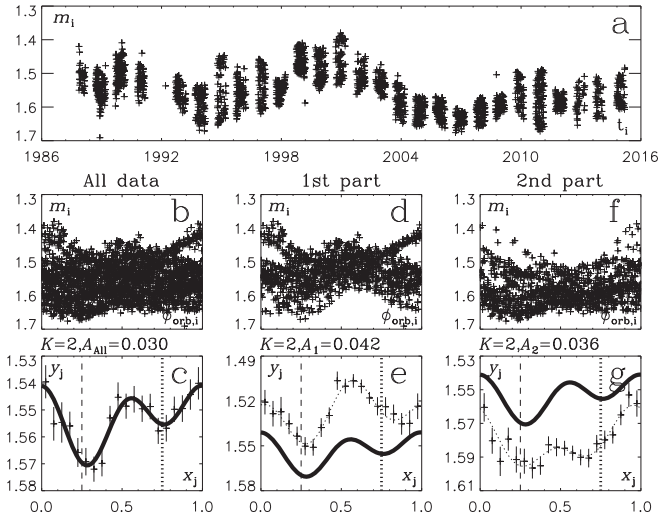

Figure 4. V711 Tau, otherwise as in Figure 1.
(The data used to create this figure are available.)

velocity epochs t_0 in Table 1. We use the radial velocity maximum epochs to compute the orbital phases from

$$\phi_{\rm orb} = {\rm FRAC}[(t - t_0)/P_{\rm orb}], \quad (1)$$

where FRAC removes the integral part of its argument (i.e., the number of full orbital rounds $P_{\rm orb}$ completed after t_0). Our value for t_0 is the Ab epoch given in Table 2.

The original data are the differential V magnitude observations $m_i = m(t_i)$, where t_i is the observing time. The time points t_i are transformed into phases $\phi_{\rm orb,i}$ (Equation (1)). The m_i observations are binned in phase, using $N = 20$ evenly spaced bins, where the limits of the jth bin are $(j-1)/N \leqslant \phi_{{\rm orb},i} < j/N$. A bin must contain at least two m_i values. The binned data for the n_j values of m_i in the jth bin are $x_j = (j/N) - 1/(2N)$, $y_j = n_j^{-1}\sum_{i=1}^{n_j} m_i$, $\sigma_j = n_j^{-1/2}[n_j^{-1}\sum_{i=1}^{n_j}(m_i - y_j)^2]^{1/2} = n_j^{-1}[\sum_{i=1}^{n_j}(m_i - y_j)^2]^{1/2}$.

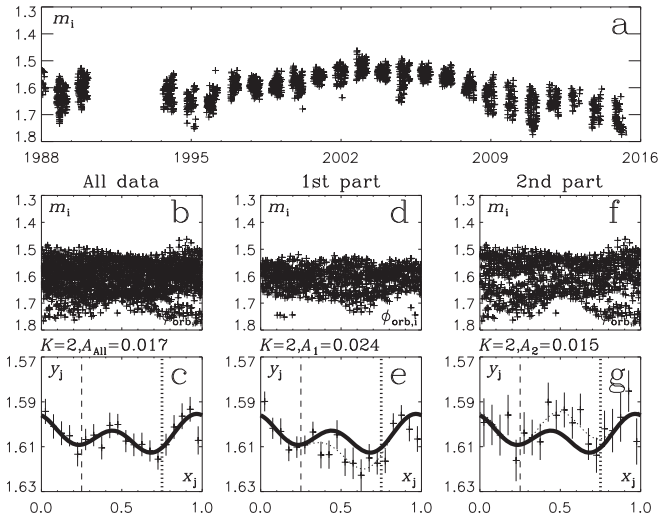

Figure 5. EI Eri. Note that the deeper primary minimum shifts from $\phi_{\rm orb} \approx 0.65$ to ≈ 0.20 (eg); otherwise as in Figure 1.
(The data used to create this figure are available.)

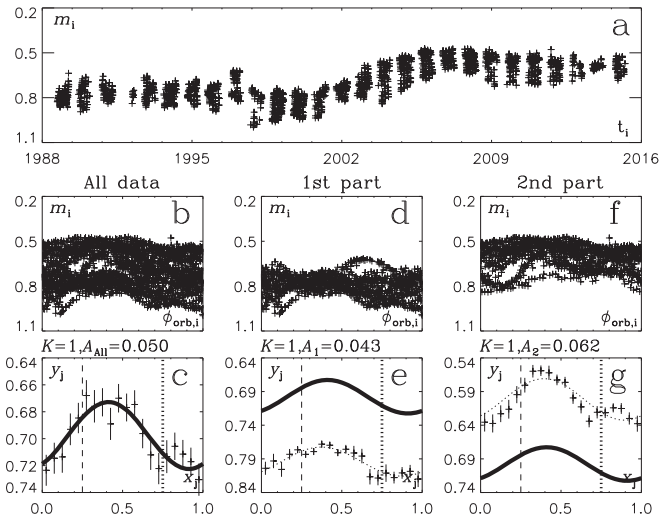

Figure 6. V1149 Ori. Notice the dip in (ceg), at $\phi_{\rm orb} \approx 0.75$; otherwise as in Figure 1.
(The data used to create this figure are available.)

The model for these data is

$$g(x, \bar{\beta}) = a_0 + \sum_{k=1}^{K} a_k \cos(kx) + b_k \sin(kx), \quad (2)$$

where $\bar{\beta} = [a_0, a_1, ..., a_K, b_1, \ldots, b_K]$ are the free parameters. Note that the model is simply $g(x, \bar{\beta}) = a_0$, if $K = 0$. The model residuals $\epsilon_j = y_j - g(x_j, \bar{\beta})$ give $\chi^2(\bar{y}, \bar{\beta}) = \sum_{j=1}^{N} w_j \epsilon_j^2$, where $w_j = \sigma_j^{-2}$.

The main question is, do these data contain a periodic signal? And if so, what is the correct order K for the model of this signal? We solve this problem, as Lehtinen et al. (2011) did, by computing the Bayesian information criterion parameter

$$R_{\rm BIC} = 2n \ln \lambda(\bar{y}, \bar{\beta}) + (5K + 1) \ln n, \quad (3)$$

where $\lambda(\bar{y}, \bar{\beta}) = \chi^2(\bar{y}, \bar{\beta}) [\sum_{j=1}^{N} w_j]^{-1}$. This parameter can be used to decide which particular order K gives the best model for the data. The value of $R_{\rm BIC}$ increases for both too low or too high incorrect values of K. The best modeling order K for the data is the value of the order that minimizes $R_{\rm BIC}$. We test the values $K = 0$, 1, and 2 for the binned data of each CABS. The best K value for the MLC of all data of each star, and the peak to peak amplitude $A_{\rm All}$ of this MLC, are given in Table 1. The periodic MLC phenomenon is present in all 14 CABS (i.e., $K \geqslant 1$).

We divide the data into two parts in our Figures 1–14. This allows us to check the stability of MLC (i.e., if the starspot distribution changes, then MLC changes). The first and second parts of the data are before and after $t_1 + \Delta T/2$, respectively. The order K of the MLC model for the first and second part of the data is fixed to the K value obtained for all data. However, the amplitudes of these MLC models, A_1 and A_2, are determined separately from a fit to the binned data of the first and second part of the data. We use the notation ΔA for the maximum difference between the three amplitudes $A_{\rm All}$, A_1, and A_2.

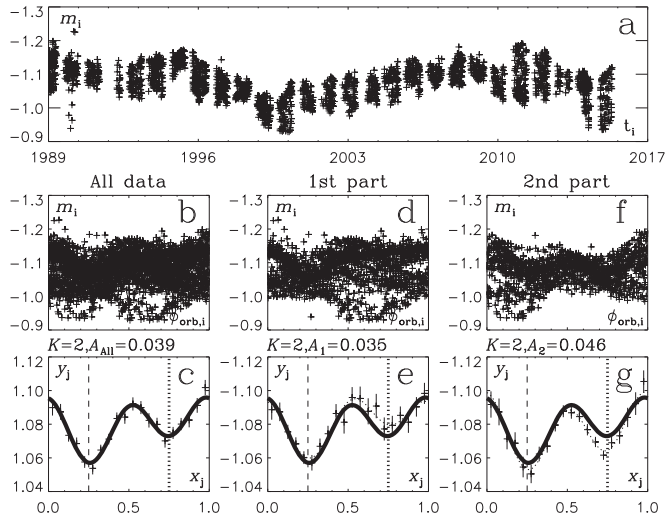

Figure 7. σ Gem, otherwise as in Figure 1.
(The data used to create this figure are available.)

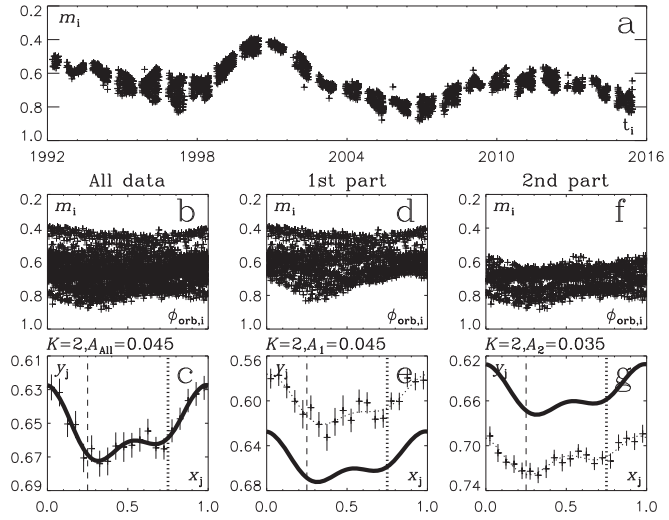

Figure 8. FG UMa; otherwise as in Figure 1.
(The data used to create this figure are available.)

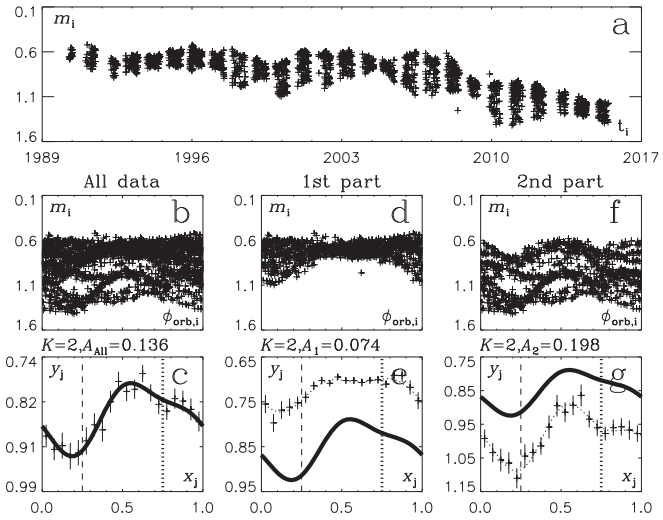

Figure 9. HU Vir; otherwise as in Figure 1.
(The data used to create this figure are available.)

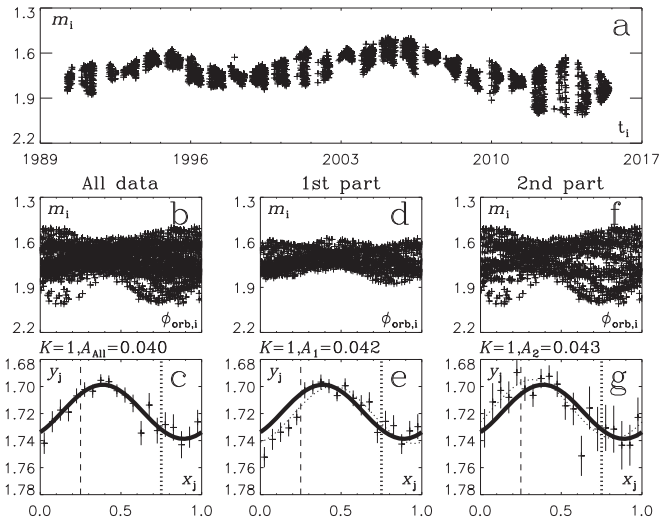

Figure 10. BM CVn; otherwise as in Figure 1.
(The data used to create this figure are available.)

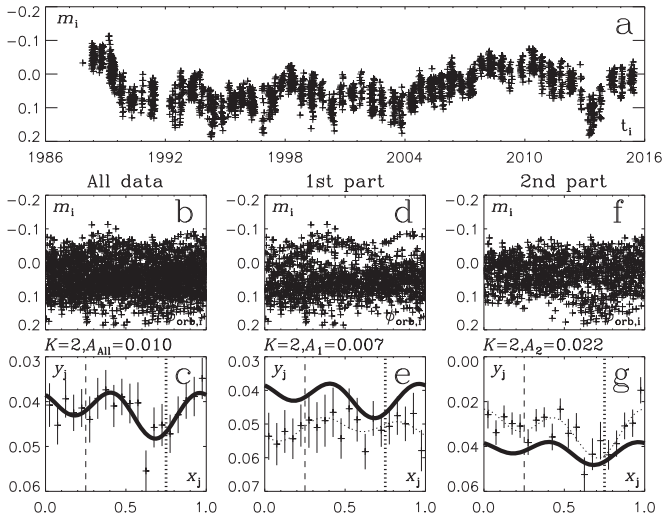

Figure 11. V478 Lyr. Note that the deeper primary minimum shifts from $\phi_{\rm orb} \approx 0.10$ to $\approx$0.60 (eg); otherwise as in Figure 1.
(The data used to create this figure are available.)

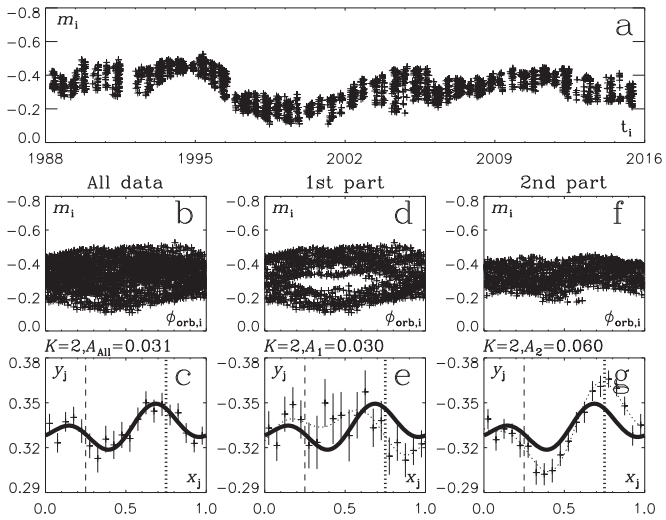

Figure 12. V1762 Cyg; otherwise as in Figure 1. Note that the deeper primary minimum shifts from $\phi_{\rm orb} \approx 0.90$ to $\approx$0.40 (eg).
(The data used to create this figure are available.)

The orbital ephemeris epoch (t_0), the orbital period (P_0), the eccentricity (e), and the spectral type of component A of CABS information in Tables 1 and 2 is from Eker et al. (2008; the third catalogue of CABS). The original references for this information are given in Section 4, where the results for each individual star are discussed separately.

4. MLC Analysis Results

Here we describe the MLC of each individual CABS and give the original references for their physical parameters in Tables 1 and 2.

4.1. MLC of DM UMa

The high amplitude, $A_{\rm All} = 0\overset{\rm m}{.}071$, sinusoidal MLC of DM UMa remains nearly unchanged between $0.4 < \phi_{\rm orb} < 0.6$ (Figures 1(c), (e) and (g)). The largest MLC changes occur between Aa $\equiv -0.25 < \phi_{\rm orb} < 0.25 \equiv$ Ac. MLC level, shape, and phase are nearly stable. MLC amplitude changes are small ($\Delta A = 0\overset{\rm m}{.}013$). MLC minimum coincides with Aa (Crampton et al. 1979; Glebocki & Stawikowski 1995; Barrado y Navascues et al. 1998; Hatzes 1998, $P_{\rm orb}$, t_0, e, Sp-type of component A).

4.2. MLC of XX Tri

The sinusoidal MLC of XX Tri has an extremely high amplitude of $A_{\rm All} = 0\overset{\rm m}{.}136$. This variation increases to $A_1 = 0\overset{\rm m}{.}233$ during the first part of that data, and then decreases to $A_2 = 0\overset{\rm m}{.}025$ in the second part. Despite these dramatic changes, the MLC phase remains stable. MLC minimum and maximum phases coincide with Aa and Ac epochs (Strassmeier & Olah 1992; Bopp et al. 1993; Strassmeier 1999, $P_{\rm orb}$, t_0, e, Sp-type of component A). Note

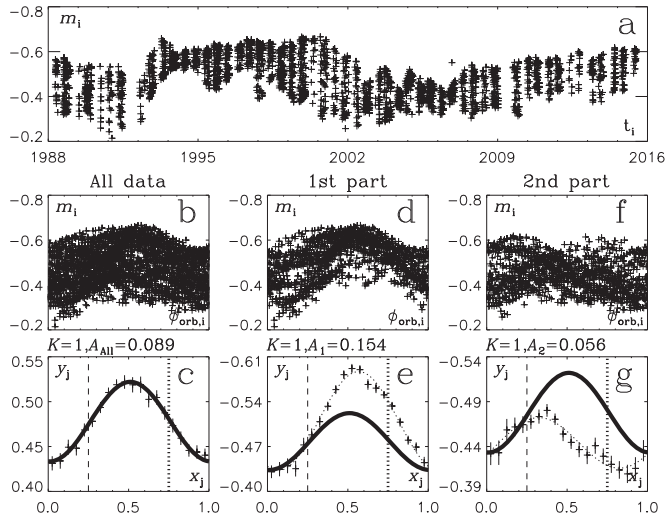

Figure 13. HK Lac; otherwise as in Figure 1.
(The data used to create this figure are available.)

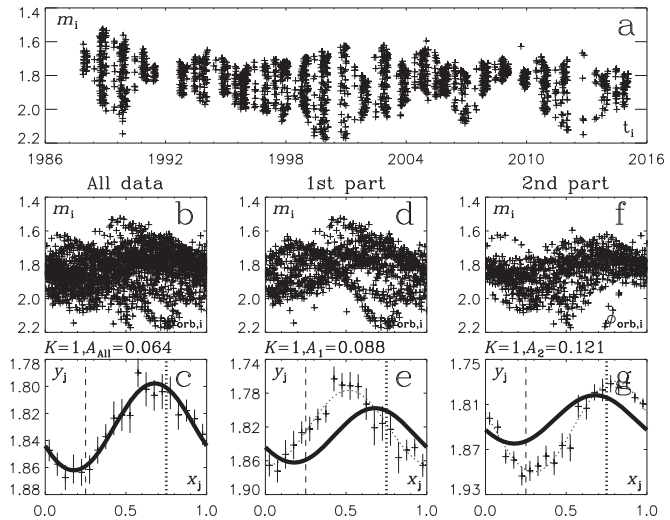

Figure 14. II Peg, otherwise as in Figure 1.
(The data used to create this figure are available.)

the minor MLC dips at $\phi_{\rm orb} = 0.25$ and 0.75 in Figure 2(g), which will be discussed in Section 6.1.4.

4.3. MLC of EL Eri

EL Eri has a sinusoidal MLC with an amplitude of $A_{\rm All} = 0\overset{\rm m}{.}048$ (Figure 3(c)). MLC shape, amplitude, and phase remain quite stable ($\Delta A = 0\overset{\rm m}{.}018$), despite the large mean level changes between the first and second part of the data (Figures 3(c)–(g)). The Aa and Ac epochs nearly coincide with the MLC maximum and minimum (Fekel et al. 1986; Balona 1987, $P_{\rm orb}$, t_0, e, Sp-type of component A).

4.4. MLC of V711 Tau

The double-peaked MLC of V711 Tau has a low amplitude (Figure 4; $A_{\rm All} = 0\overset{\rm m}{.}030$). This amplitude remains quite stable (Figures 4(c), (e), and (g); $\Delta A = 0\overset{\rm m}{.}012$), regardless of the changes in the mean level (Figures 4(d) and (f)). The MLC primary minimum phase $\phi_{\rm orb} = 0.25$ does not shift, but the

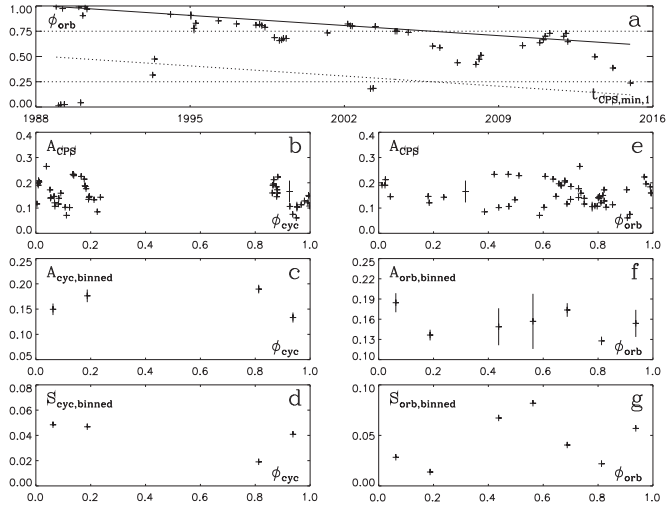

Figure 15. DM UMa. (a) Orbital phases $\phi_{\rm orb}$ for primary minima $t_{\rm CPS,min,1}$ (note that error bars are shown, but they are smaller than symbol size), orbital phases $\phi_{\rm orb} = 0.25$ and 0.75 (dotted lines), active longitude phases $\phi_{\rm orb} = 0$ (continuous line), and 0.50 (dashed line). (b) All amplitudes $A_{\rm CPS}$ vs. $\phi_{\rm cyc}$. (c) Binned amplitudes $A_{\rm cyc,binned}$ vs. $\phi_{\rm cyc}$. (d) Binned standard deviations $S_{\rm cyc,binned}$ vs. $\phi_{\rm cyc}$. (e) All amplitudes $A_{\rm CPS}$ vs. $\phi_{\rm orb}$. (f) Binned amplitudes $A_{\rm orb,binned}$ vs. $\phi_{\rm orb}$. (g) Binned standard deviations $S_{\rm orb,binned}$ vs. $\phi_{\rm orb}$.

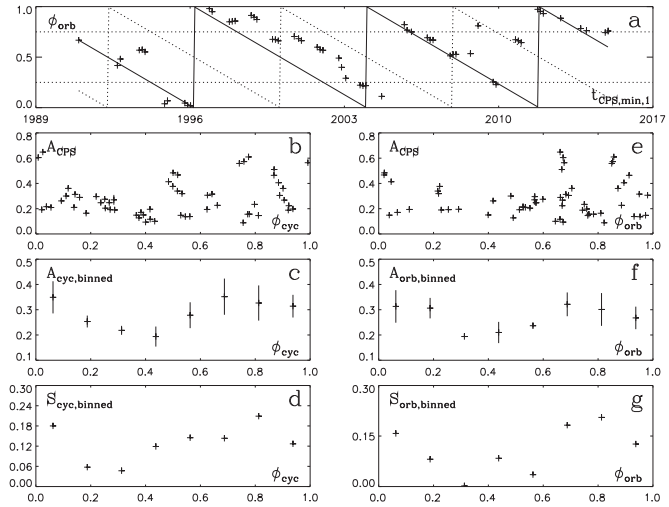

Figure 16. XX Tri; otherwise as in Figure 15.

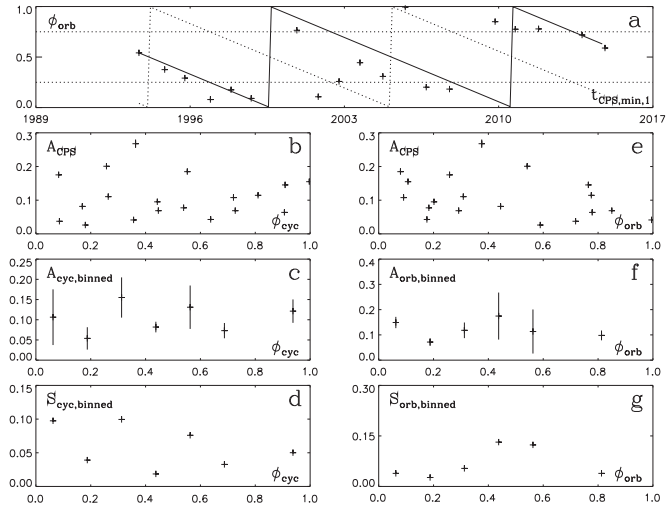

Figure 17. EL Eri; otherwise as in Figure 15.

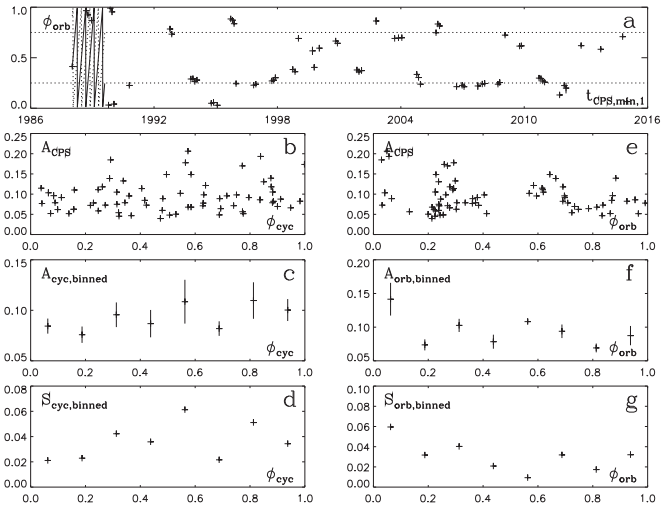

Figure 18. V711 Tau; otherwise as in Figure 15.

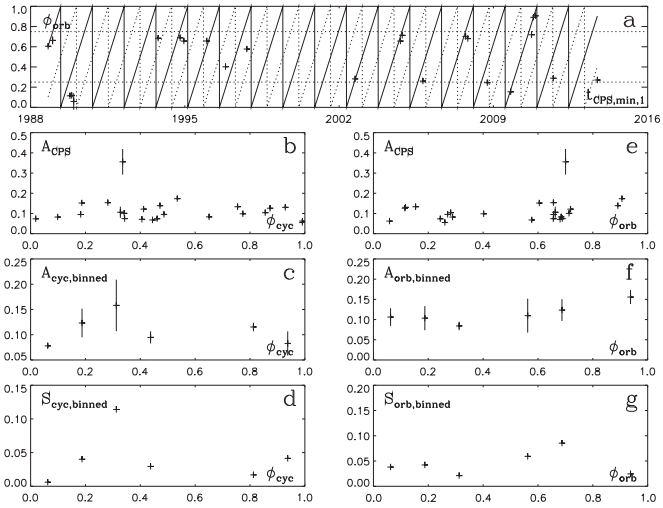

Figure 19. EI Eri; otherwise as in Figure 15.

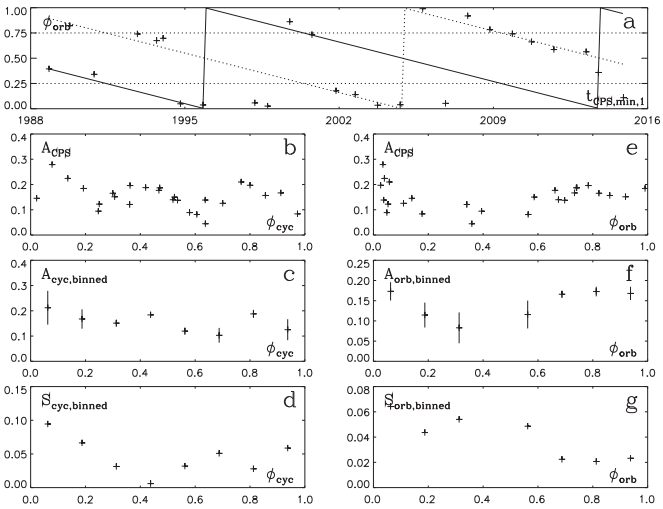

Figure 20. V1149 Ori; otherwise as in Figure 15.

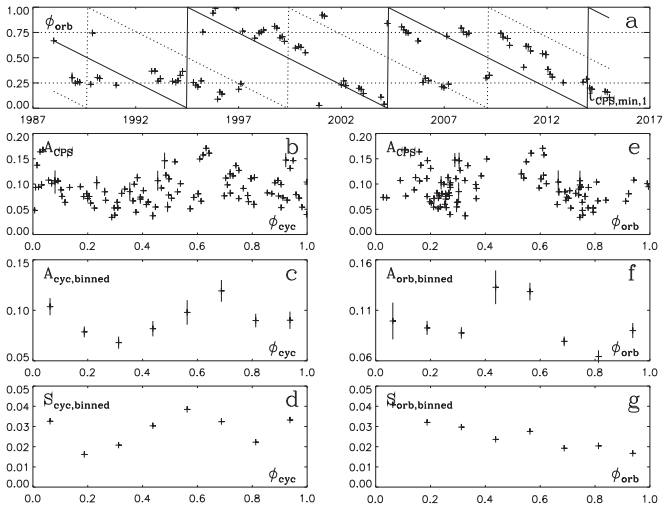

Figure 21. σ Gem; otherwise as in Figure 15.

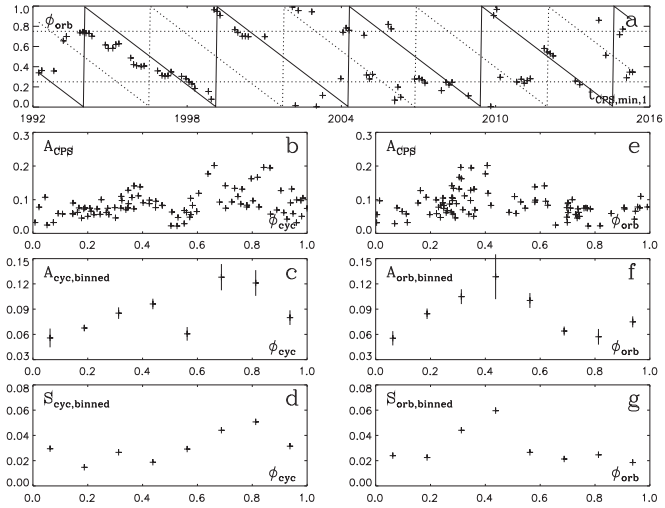

Figure 22. FG UMa; otherwise as in Figure 15.

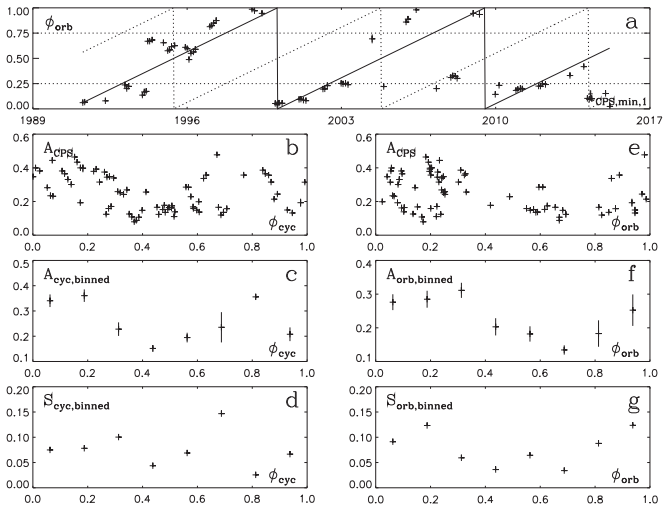

Figure 23. HU Vir; otherwise as in Figure 15.

secondary minimum $\phi_{\rm orb} = 0.8$ in the first part shifts to 0.7 in the second part. The epochs of Ac and Aa coincide with the MLC primary and secondary minima (Fekel 1983; Donati et al. 1992; García-Alvarez et al. 2003; $P_{\rm orb}$, t_0, e, Sp-type of component A). However, the interpretation of this MLC may be more complicated, because the hotter component B (G5 IV) could also influence MLC (Fekel 1983; García-Alvarez et al. 2003).

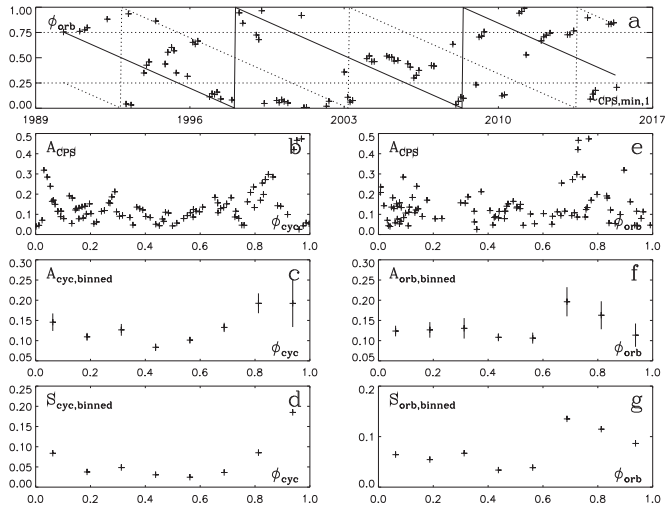

Figure 24. BM CVn; otherwise as in Figure 15.

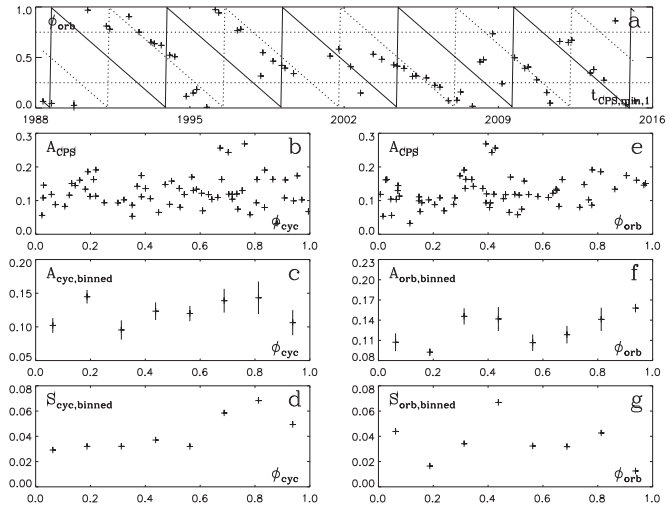

Figure 25. V1762 Cyg; otherwise as in Figure 15.

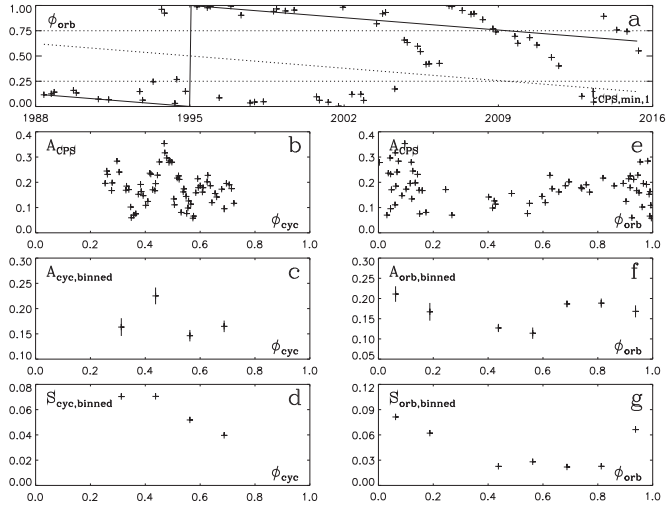

Figure 26. HK Lac; otherwise as in Figure 15.

4.5. MLC of EI Eri

EI Eri has a very stable low amplitude double-peaked MLC (Figure 5(a): $A_{\rm All} = 0\overset{\rm m}{.}017$). MLC mean and amplitude do not change. Only minor MLC changes occur in the interval $0.25 < \phi_{\rm orb} < 0.75$. MLC primary minimum at $\phi_{\rm orb} = 0.65$ in the first part of the data shifts to $\phi_{\rm orb} = 0.20$ in the second part. Epochs of Ac and Aa occur about $\Delta\phi_{\rm orb} = 0.05$ after MLC secondary and primary minima (Fekel et al. 1986, 1987; Strassmeier 1990; Cutispoto 1995; $P_{\rm orb}$, t_0, e, Sp-type of component A).

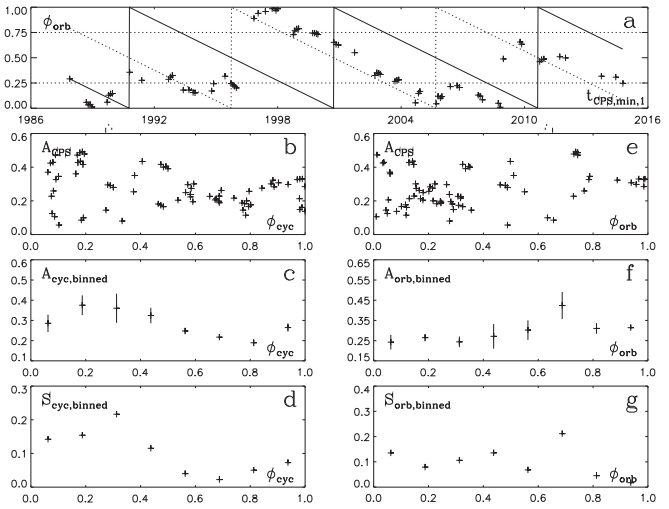

Figure 27. II Peg; otherwise as in Figure 15.

4.6. MLC of V1149 Ori

V1149 Ori has a sinusoidal MLC with an amplitude of $A_{\rm All} = 0\overset{\rm m}{.}050$ (Figure 6(c)). MLC amplitude, shape, and minimum are stable (Figures 6(c), (e), and (g), $\Delta A = 0\overset{\rm m}{.}012$), although MLC mean changes are large (Figures 6(d) and (f)). Epochs of Ac and Aa occur about $\Delta\phi_{\rm orb} = 0.15$ before MLC maximum and minimum (Hall et al. 1991; Fekel & Henry 2005, $P_{\rm orb}$, t_0, e, Sp-type of component A). Note the MLC dip at about $\phi_{\rm orb} = 0.75$ in Figures 6(c), (e), and (g), which will be discussed later in Section 6.1.4.

4.7. MLC of σ Gem

σ Gem has a stable double-peaked MLC with an amplitude of $A_{\rm All} = 0\overset{\rm m}{.}039$ (Figure 7, $\Delta A = 0\overset{\rm m}{.}011$). MLC mean, amplitude, minimum, and maximum do not change. Small changes are seen only in the interval $0.50 < \phi_{\rm orb} < 0.75$. MLC primary and secondary minima coincide with the Ac and Aa epochs (Strassmeier et al. 1988; Bopp & Dempsey 1989; Duemmler et al. 1997, $P_{\rm orb}$, t_0, e, Sp-type of component A).

4.8. MLC of FG UMa

FG UMa has a stable second order MLC ($K = 2$). MLC amplitude is about constant ($\Delta A = 0\overset{\rm m}{.}010$). The double-peaked shape and phase of this MLC is the same in Figures 8 (c), (e), and (g), although the mean levels of the first and second part of the m_i data are different in Figures 8(d) and (f). The activity level changes only alter the MLC mean, but not the MLC shape, minimum, maximum, or amplitude. MLC primary and secondary minima nearly coincide with Ac and Aa (Fekel et al. 2002, $P_{\rm orb}$, t_0, e, Sp-type of component A).

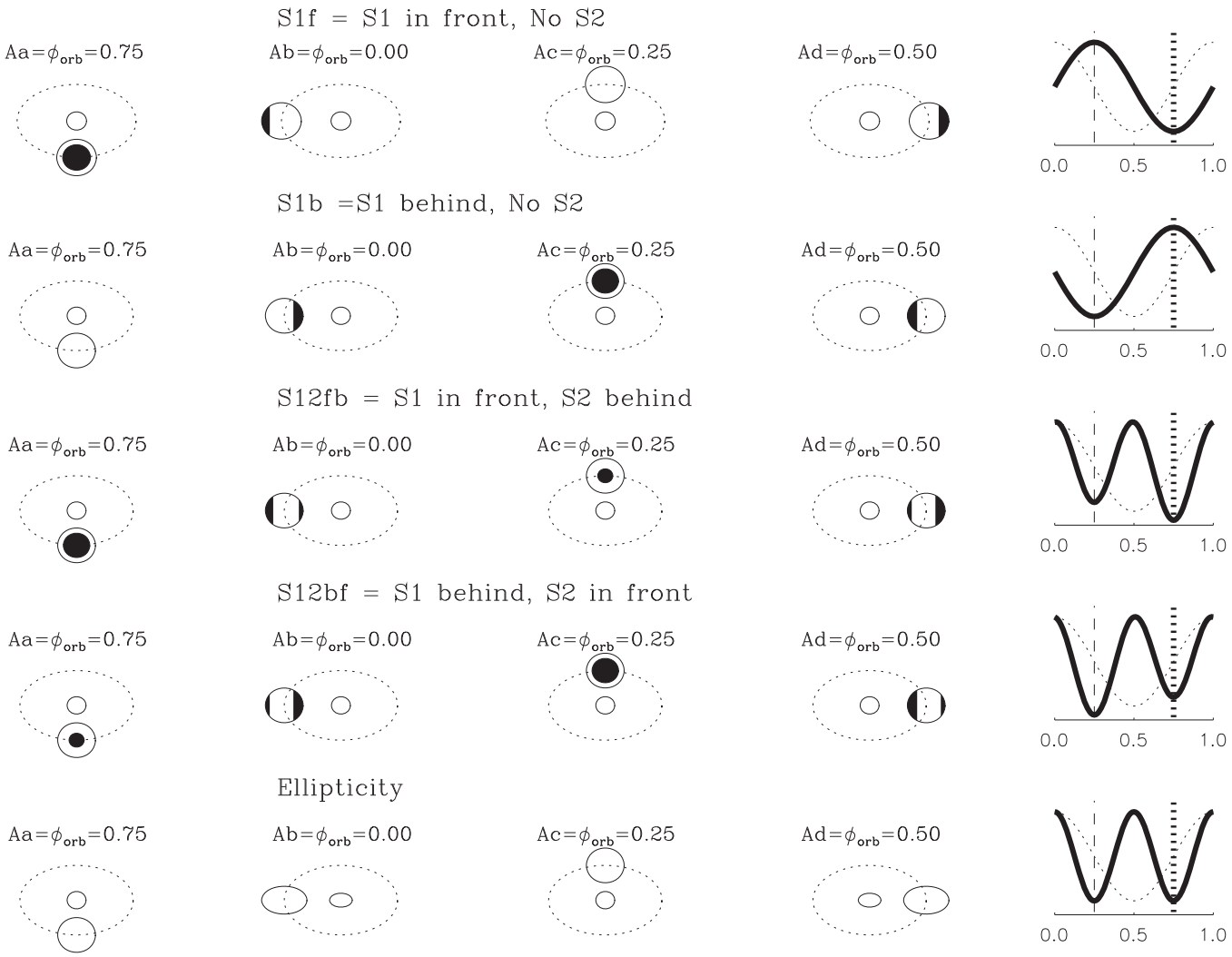

Figure 28. Stationary "flip-flop." The highest line: four first sketches show the S1f mode configuration of CABS at epochs Aa, Ab, Ac, and Ad, described in Section 6.1. The fifth sketch shows the qualitative changes of radial velocity (dashed line) and MLC (thick continuous line) in an arbitrary scale. Vertical lines indicate epochs Aa (thick dotted line) and Ac (thin dashed line). The second, third, and fourth highest lines: S1b, S12fg, and S12bf mode configurations; otherwise as in the highest line. Lowest line: ellipticity configurations at Aa, Ab, Ac, and Ad epoch. Radial velocity and MLC curves are as in the highest line.

4.9. MLC of HU Vir

HU Vir has a high amplitude, $A_{All} = 0\overset{m}{.}136$, second-order MLC with a nearly sinusoidal shape (Figure 9(c)). MLC amplitude is smaller in the first part, $A_1 = 0.074$, and increases to an extreme value $A_2 = 0.198$ in the second part. The Ac epoch is close to MLC primary minimum, while Aa is close to a weak secondary minimum, which is more clearly visible in Figure 9(g) for the second part (Cutispoto 1993; Fekel et al. 1999, P_{orb}, t_0, e, Sp-type of component A).

4.10. MLC of BM CVn

BM CVn has a stable sinusoidal MLC (Figures 10(c), (e), and (g)). Small MLC changes occur in the $-0.10 < \phi_{orb} < 0.40$ interval, but none in the $0.40 < \phi_{orb} < 0.90$ interval. Aa and Ac epochs are about $\Delta\phi_{orb} = 0.15$ before the MLC minimum and maximum (Griffin & Fekel 1988; Koen & Eyer 2002, P_{orb}, t_0, e, Sp-type of component A).

4.11. MLC of V478 Lyr

MLC of V478 Lyr is double-peaked and has a very low amplitude of $A_{All} = 0\overset{m}{.}010$. MLC shape and amplitude do not change a lot (Figures 11(c), (e), and (g), $\Delta A = 0\overset{m}{.}015$), although the activity levels do (Figures 11(d) and (f)). The MLC primary minimum at $\phi_{orb} = 0.10$ in the first part shifts to $\phi_{orb} = 0.65$ in the second part. The Ac and Aa epochs occur about $\Delta\phi_{orb} = 0.1$ after MLC secondary and primary minima (Griffin & Fekel 1988; Fekel 1988, P_{orb}, t_0, e, Sp-type of component A).

4.12. MLC of V1762 Cyg

V1762 Cyg has a double-peaked MLC with $A_{All} = 0\overset{m}{.}031$ (Figure 12(c)). MLC mean is stable, but MLC amplitude changes occur ($\Delta A = 0\overset{m}{.}030$). The deeper MLC primary minimum at $\phi_{orb} \approx 0.4$ in the first part shifts to $\approx\phi_{orb} = 0.9$ in the second part (Figures 12(e) and (g)). This switch will be discussed in Section 6.1.5. MLC is stable only in the short interval $0.00 < \phi_{orb} < 0.15$. The Ac epoch occurs about

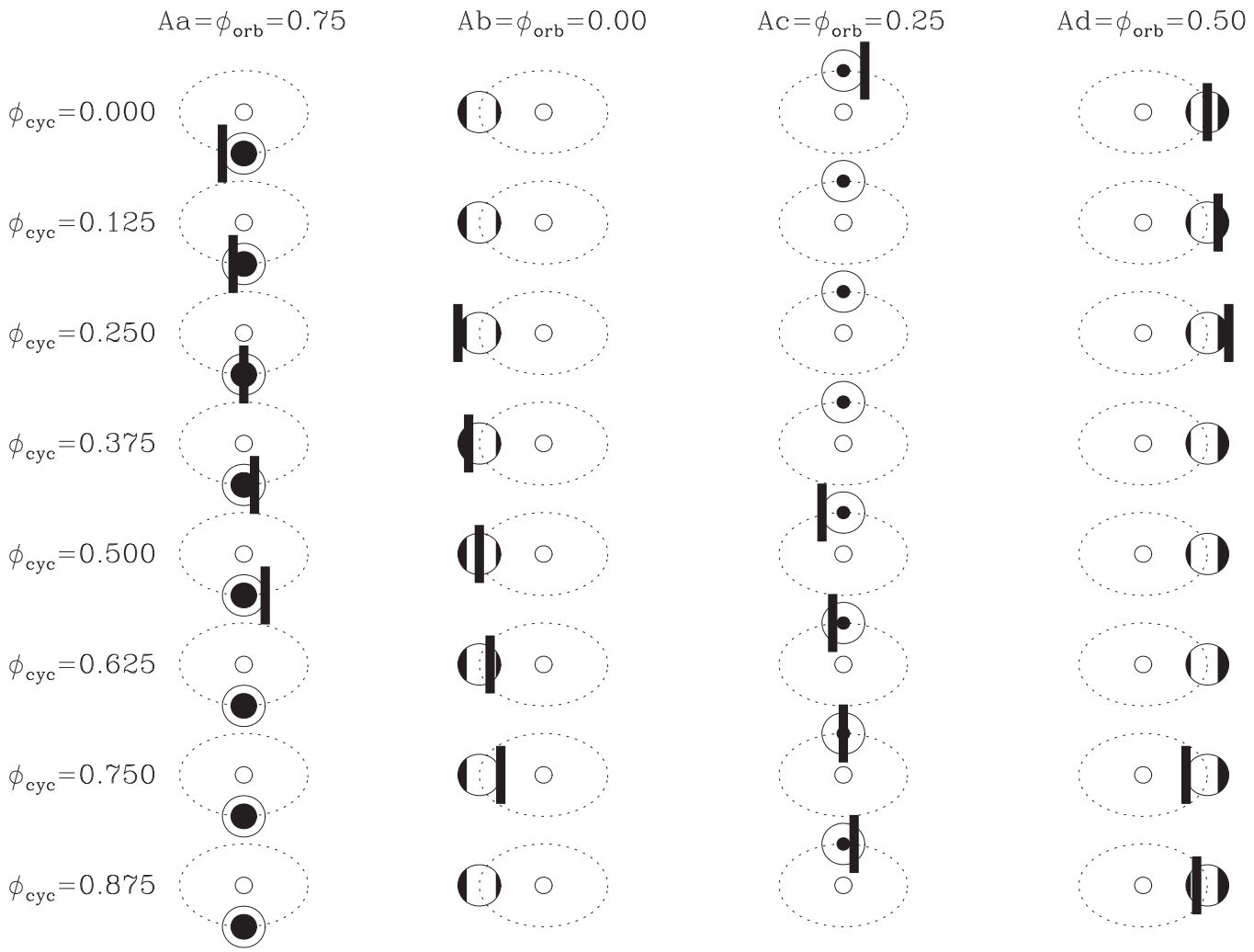

Figure 29. One complete P_{cyc} lap cycle. Lap cycle phases ϕ_{cyc} are given on the left of each line. Nonstationary spot S3 (Equation (7)) rotates once around component A during P_{Cyc}. A thick dark vertical line denotes the longitude of spot S3 on component A. We mark this longitude only when spot S3 is visible on stellar disk of component A. Locations of stationary spots S1 and S2 (Equation (8)) are as on the third line of Figure 28.

$\Delta\phi_{orb} = 0.15$ before MLC primary minimum, while Aa remains close to the MLC maximum (Osten & Saar 1998, P_{orb}, t_0, e, SP-type of component A).

4.13. MLC of HK Lac

HK Lac has a high amplitude, $A_{All} = 0\overset{m}{.}089$, sinusoidal MLC, which remains stable at $0.00 \leqslant \phi_{orb} \leqslant 0.30$ (Figures 13 (c), (e), and (g)). Its amplitude increases to $A_1 = 0\overset{m}{.}154$ during the first part of the data and decreases to $A_2 = 0\overset{m}{.}056$ during the second part. The MLC minimum and shape remain nearly unchanged. Epochs Ac and Aa coincide with MLC maxima and minima in Figure 13(g) during the second part of the data (Gorza & Heard 1971; Özeren et al. 1999; Koen & Eyer 2002; Cardini 2005, P_{orb}, t_0, e, Sp-type of component A).

4.14. MLC of II Peg

II Peg has a sinusoidal MLC with a relatively large amplitude, $A_{All} = 0\overset{m}{.}064$ (Figure 14(c)). The amplitude is $A_1 = 0\overset{m}{.}088$ in the first part of the data, and then increases to $A_2 = 0\overset{m}{.}121$ in the second part. The MLC minimum and maximum phases are close to Ac and Aa in Figure 14(c), but they shift $\Delta\phi_{orb} = -0.2$ backward in the first part of the data, and then return back to phases $\phi_{orb} = 0.3$ and 0.8 in the second part (Berdyugina et al. 1998, P_{orb}, t_0, e, Sp-type of component A).

5. CPS Analysis Results

Next, we apply the continuous period search (Lehtinen et al. 2011; hereafter CPS) to the differential V magnitudes of our 14 CABS. This gives us the following seasonal short-term light curve parameters:

$M_{CPS}(\tau_{CPS})$ = Mean level of brightness
$A_{CPS}(\tau_{CPS})$ = Peak to peak amplitude
$P_{CPS}(\tau_{CPS})$ = Photometric rotation period
$t_{CPS,min,1}(\tau_{CPS})$ = Primary minimum epoch in time
$t_{CPS,tmin,2}(\tau_{CPS})$ = Secondary minimum epoch in time

where τ_{CPS} is the mean of all observing times t_i of y_i of the modeled data set. Lehtinen et al. (2011) formulated this method. It has been applied to the photometry of numerous stars (e.g., Hackman et al. 2011; Kajatkari et al. 2014; Lehtinen et al. 2016), and it is therefore not described here in greater detail. We use only the results for independent and reliable data sets. "Independent" means that the modeled data sets do not overlap (i.e., they have no common y_i values). The meaning of

Table 1
CABS Sample

1. Variable	2.	3. Comparison	4. Beg	5. End	6. ΔT (years)	7. n	8. $P_{\rm orb}$ (days)	9. t_0 [HJD-2400000]	10. e	11. K	12. $A_{\rm All}$ (mag)
DM UMa	SAO 15334	HD 95362	29.10.1988	13.6.2015	26.6	1915	7.492 ± 0.009	43881.4 [*a*]	0	1	0.071
XX Tri	HD 12545	HD 12478	7.10.1990	13.2.2015	24.4	1962	23.96924 ± 0.00092	47814.315 [*a*]	0	1	0.136
EL Eri	HD 19754	HD 19421	19.10.1990	11.2.2015	24.3	1642	48.263 ± 0.206	44419.9 [*b*]	0.1	1	0.048
V711 Tau	HD 22468	HD 22484	13.11.1987	11.3.2015	27.3	2293	2.83774 ± 0.00001	51142.943 [*c*]	0	2	0.030
EI Eri	HD 26337	HD 26409	11.1.1988	7.3.2015	27.2	2268	1.947227 ± 0.000008	46091.052 [*a*]	0	2	0.017
V1149 Ori	HD 37824	HD 38309	13.9.1988	28.3.2015	26.5	2274	53.57465 ± 0.00072	48625.022 [*a*]	0	1	0.050
σ Gem	HD 62044	HD 60318	21.11.1987	1.5.2015	27.4	2984	19.604471 ± 0.000022	47227.15 [*d*]	0.012	2	0.039
FG Uma	HD 89546	HD 90400	15.3.1992	11.6.2015	23.2	3145	21.35957 ± 0.00040	49297.702 [*a*]	0	2	0.045
HU Vir	HD 106225	HD 105796	6.4.1990	15.6.2015	25.2	2062	10.387552 ± 0.000031	49993.195 [*b*]	0.0093	2	0.136
BM CVn	HD 116204	HD 116010	6.4.1990	17.6.2015	25.2	2917	20.6252 ± 0.0018	45251.62 [*a*]	0	1	0.040
V478 Lyr	HD 178450	HD 177878	14.11.1987	21.6.2015	27.6	2641	2.130514 ± 0.000007	45939.801 [*a*]	0	2	0.010
V1762 Cyg	HD 179094	HD177483	25.4.1988	21.6.2015	27.2	2526	28.58973 ± 0.00002	31043.408 [*a*]	0	2	0.031
HK Lac	HD 209813	HD 210731	30.4.1988	21.6.2015	27.1	2454	24.4284 ± 0.0005	40017.17 [*b*]	0.01	1	0.089
II Peg	HD 224085	HD 224930	16.11.1987	23.1.2015	27.2	2049	6.724333 ± 0.000010	49582.9268 [*e*]	0	1	0.064

Note. Variable (columns 1 and 2, variable designation and HD or SAO number), comparison star (column 3, SAO or HD number), first and last observing date (columns 4 and 5, beginning and end), time span and number of observations (columns 6 and 7, [ΔT] = years and n), orbital period, epoch, and eccentricity (columns 8–10, $P_{\rm orb}$ = days, t_0, and e, epoch types: [*a*] = radial velocity maximum, [*b*] = periastron, [*c*] = cool in front, [*d*] = primary in front, [*e*] = primary behind), MLC order, and amplitude (columns 11 and 12, K and [$A_{\rm All}$] = mag).

Table 2
CABS Sample

1. Variable	2.	3. Sp-type of A	4. Aa	5. Ab	6. Ac
DM UMa	SB1	K0–1 IV–III	43879.527	43881.400	43883.273
XX Tri	SB1	K0 III	47808.323	47814.315	47820.307
EL Eri	SB1	G8 III–IV	44419.966	44432.032	44444.097
V711 Tau	SB2	K1 IV	51142.943	51143.652	51144.362
EI Eri	SB1	G5 IV	46090.565	46091.052	46091.539
V1149 Ori	SB1	K0 III	48611.628	48625.022	48638.416
σ Gem	SB1	K1 III	47227.150	47232.051	47236.952
FG Uma	SB1	G9 III	49292.362	49297.702	49303.042
HU Vir	SB1	K2 III	49993.403	49996.000	49998.597
BM CVn	SB1	G8 III	45246.464	45251.620	45256.776
V478 Lyr	SB1	G8 V	45939.268	45939.801	45940.334
V1762 Cyg	SB2	K2 IV–III	31036.261	31043.408	31050.555
HK Lac	SB1	K0 III	40011.066	40017.173	40023.281
II Peg	SB1	K2 V	49579.565	49581.246	49582.927

Note. Variable (column 1), single-lined (SB1) or double-lined (SB2), Sp-type of component A, epochs Aa, Ab, and Ac [HJD-2400000] (columns 2–6).

Table 3
Active Longitude

1. Variable	2. n	3. P_{act} (days)	4. Q_K	5. $t_{cyc,0}$ (HJD)	6. P_{cyc} (days)	7. P_{cyc} (years)
DM UMa	54	7.4898 ± 0.0008	3×10^{-11}	47499.990	25506 ± 104725	69.8
XX Tri	59	23.77 ± 0.01	2×10^{-11}	48237.800	2860 ± 145	7.8
EL Eri	19	47.69 ± 0.02	0.0006	49236.206	4017 ± 1434	11.0
V711 Tau	70	2.8924 ± 0.0002	0.003	47171.961	150 ± 1	0.4
EI Eri	24	1.9545 ± 0.0008	0.008	47453.341	526 ± 58	1.4
V1149 Ori	26	53.14 ± 0.06	0.02	47467.507	6550 ± 912	17.9
σ Gem	97	19.497 ± 0.005	2×10^{-8}	47166.728	3557 ± 166	9.7
FG Uma	91	21.12 ± 0.01	2×10^{-6}	48706.889	1883 ± 80	5.2
HU Vir	74	10.419 ± 0.001	1×10^{-8}	48355.411	3438 ± 109	9.4
BM CVn	93	20.513 ± 0.006	1×10^{-6}	47989.696	3771 ± 211	10.3
V1762 Cyg	64	28.17 ± 0.02	0.0002	47284.236	1919 ± 93	5.3
HK Lac	67	24.40 ± 0.01	4×10^{-9}	47299.669	20988 ± 7408	57.5
II Peg	77	6.7119 ± 0.0007	8×10^{-8}	47122.096	3630 ± 205	9.9

Note. Variable (column 1), number of $t_{CPS,min,1}$ estimates (column 2: n), active longitude period and its critical level (columns 3 and 4: P_{act}, Q_K), lowest $t_{CPS,min,1}$ value (column 5: [$t_{cyc,0}$])), lap cycle period of Equation (4) (columns 6 and 7: [P_{cyc}]).

"reliable" is that all model parameters (e.g., the residuals of the model) have a Gaussian distribution. The length of the modeled CPS data sets is about 1 month (i.e., we can monitor the changes of the five previously mentioned light curve parameters with this time resolution). Here we will not study the changes of M_{CPS}, P_{CPS}, and $t_{CPS,min,2}$.

Our current study concentrates on the changes of the epochs of the light curve primary minima $t_{CPS,min,1}$. These epochs are unambiguous in time (i.e., their phases are also unambiguous with any ephemeris, like Equations (1), (5) or (6)). In Figures 15–27, we will also study the amplitudes A_{CPS}, because they measure the strength of the longitudinally concentrated structures that cause the observed light curve minima $t_{CPS,min,1}$. The number of estimates obtained for these parameters are given Table 3. Very few reliable estimates are obtained for V478 Lyr ($n = 6$), because its photometric rotation period is very close to 2.1 days. It is difficult to get an adequate phase coverage within 30 days before its light curve changes. Therefore the analysis of this CABS stops here.[4]

[4] All $t_{CPS,min,1}$ and A_{CPS} results for the remaining 13 CABS are published electronically at the Vizier database.

We apply the non-weighted Kuiper test formulated in Jetsu & Pelt (1996) to the primary minima $t_{CPS,min,1}$ of the remaining 13 CABS. The tested period interval is ±15% at both sides of P_{orb}. For each tested period P, we first compute the phases $\phi_i = \mathrm{FRAC}[t_i/P]$ $(i = 1, 2, \ldots n)$ for the n time points $t_i = t_{CPS,min,1}$. Then these phases ϕ_i are arranged into increasing order (i.e., into rank order $\phi_1 \leqslant \phi_2 \leqslant \ldots \leqslant \phi_n$). The monotonically increasing cumulative sample distribution function of these phases is $F_n(\phi_i) = i/n$. It is compared with a random distribution (i.e., to the cumulative sample distribution function of an even distribution $F(\phi) = \phi$). This gives the Kuiper test statistic $V_n = D^+ + D^-$, where $D^+ = \max[F_n(\phi_i) - F(\phi_i)]$ and $D^- = \max[F(\phi_i) - F_n(\phi_i)]$. If the phases ϕ_i are not evenly distributed between 0 and 1, the V_n value is large. In this case, the ϕ_i values do not represent a sample drawn from a random distribution (i.e., there is periodicity in time points t_i with the tested period P). The critical level Q_K (Jetsu & Pelt 1996, their Equation 24) represents the probability that the test statistic V_n reaches some computed value under the "null hypothesis": "ϕ_i *represent a sample drawn from a random distribution*." The results for the active longitude periods (P_{act})

and their critical levels (Q_K) are given in Table 3. The critical (Q_K) levels are significant (i.e., active longitudes definitely represent a real dominant phenomenon in these CABS). The active longitudes of V1149 Ori have the lowest significance ($Q_K = 0.02$).

We define a lap cycle period

$$P_{cyc} = |[P_{orb}^{-1} - P_{act}^{-1}]^{-1}|. \quad (4)$$

This lap cycle time interval P_{cyc} fulfills $P_{cyc}/P_{orb} - P_{cyc}/P_{rot} = \pm 1$. Any particular configuration of two structures rotating with the periods of P_{orb} and P_{act} on the surface of component A is repeated after every integer multiple of P_{cyc}, as will be illustrated later in Figure 29. The P_{cyc} cycle length increases when $|P_{orb} - P_{act}|$ difference decreases (i.e., these configurations are constantly changing), unless $P_{orb} = P_{act}$. We use the absolute value of P_{cyc}, because $P_{orb} > P_{act}$ gives a negative P_{cyc} value. The active longitudes in these CABS can rotate faster or slower than orbital motion (see Table 3, or compare Figures 21 and 23). The phases of active longitudes are

$$\phi_{act} = \mathrm{FRAC}[(t - t_{cyc,0})/P_{act}], \quad (5)$$

where $t_{cyc,0}$ is the first $t_{CPS,min,1}$ value of each CABS given in Table 3. The lap cycle phases are

$$\phi_{cyc} = \mathrm{FRAC}[(t - t_{cyc,0})/P_{cyc}]. \quad (6)$$

We compute the binned $A_{cyc,binned}(\phi_{cyc})$ values of all A_{CPS} amplitudes with respect to this phase. The standard deviations of these binned amplitudes within each bin, $S_{cyc,binned}(\phi_{cyc})$, are also computed. These standard deviations measure the scatter of A_{CPS} values within each bin. We use only 8 bins, because the total number of A_{CPS} estimates is low, typically about 50 values. We also compute the binned $A_{orb,binned}(\phi_{orb})$ values with respect to the orbital phase ϕ_{orb}, as well as the standard deviations $S_{orb,binned}(\phi_{orb})$. The phases ϕ_{orb} and ϕ_{cyc} of each A_{CPS} (Equations (1) and (6)) are computed using the $t_{CPS,min,1}$ value of the same CPS data set. The scatter cannot be large for amplitudes very close to zero, and this may introduce some bias in the interpretation of $S_{cyc,binned}$ and $S_{orb,binned}$ changes.

The results for our 13 CABS are shown in Figures 15–27. The mean of the accuracy of the orbital phases ϕ_{orb} of $t_{CPS,min,1}$ epochs in the "a" panels of these figures varies between $\sigma_\phi = 0.02$ (EI Eri) and 0.007 (V1149 Ori). The error bars of these phases are plotted in all "a" panels of Figures 15–27. These error bars are mostly smaller than the vertical size of the symbols (i.e., crosses). This means that all phase shifts larger than $\pm 3\sigma_\phi$ are certainly real events.

The P_{orb}values of some CABS are not very accurate (Table 1; e.g., DM UMa or EL Eri). There are also cases where the t_0 epoch for $\phi_{orb} = 0$ in Equation (1) is fixed to a much earlier date than the time span of our photometry (Table 1; e.g., V1762 Cyg or HK Lac). In such cases, the phases $\phi_{orb} = 0.25$ and 0.75 are not unambiguous (Figures 15–27, horizontal dotted lines). However, these two uncertainties do not interfere with the identification of "flip-flop" events (i.e., the sudden phase shifts of about 0.5 in ϕ_{orb}). Nor are these uncertainties the cause of "flip-flop" events. An error in P_{orb} changes *only* the slope of the linear migration of the ϕ_{orb} phases of $t_{CPS,min,1}$. An error in t_0 of Equation (1) adds a constant shift to *all* ϕ_{orb} phases of $t_{CPS,min,1}$. However, there would be much less "flip-flop" events if we would refer only to 180° jumps, followed by a jump back.

5.1. Active Longitudes and Amplitudes of DM UMa

The lap cycle of DM UMa is long, $P_{cyc} = 69.8$ years, but this value is very uncertain, because the error of P_{orb} is so large (Tables 1 and 3). The migration of the $t_{CPS,min,1}$ phases is regular, except for the two "flip-flop" events that occurred in the years 1993 and 2003. This regular migration becomes irregular when the active longitude crosses the orbital period phase $\phi_{orb} = 0.75$ (Figure 15(a), crossing continuous and dotted lines). However, the P_{orb} value is so inaccurate that this $\phi_{orb} = 0.75$ level is not unambiguous. The gap with no data in Figure 15(b) awaits for the missing future observations. The connection between A_{CPS} and ϕ_{orb} is not clear (Figures 15(b)). We get only four binned $A_{cyc,binned}(\phi_{cyc})$ and $S_{cyc,binned}(\phi_{cyc})$ values (Figures 15(c) and (d)). The seven $A_{orb,binned}$ values (Figure 15(f)) show a regular connection to ϕ_{orb}, which is confirmed by the $S_{orb,binned}$ changes (Figures 15(g)).

5.2. Active Longitudes and Amplitudes of XX Tri

The lap cycle of XX Tri, $P_{cyc} = 7.8$ years, is accurate (Table 3). It is clearly not the cycle of the mean brightness (Figure 2(a)). The active longitude is very stable (Figure 16(a)). There are some migration irregularities, especially when the active longitude migrates across orbital phases $\phi_{orb} = 0.25$ and 0.75 in the years 1998 and 2010. After the latter crossing, two "flip-flop" events occur in the years 2011 and 2012. The changes of $A_{CPS}(\phi_{cyc})$ are very regular, as well as those of $A_{cyc,binned}(\phi_{cyc})$ and $S_{cyc,binned}(\phi_{cyc})$ (Figures 16(b), (c), and (d)). The $A_{CPS}(\phi_{orb})$, $A_{orb,binned}(\phi_{orb})$, and $S_{orb,binned}(\phi_{orb})$ changes are also regular (Figures 16(f), (e), and (g)).

5.3. Active Longitudes and Amplitudes of EL Eri

Very few $t_{CPS,min,1}$ and $A_{CPS,min,1}$ estimates of EL Eri are available ($n = 19$). The active longitude migration in the $t_{CPS,min,1}$ phases is stable before the year 2000, when the active longitude crosses the orbital phase $\phi_{orb} = 0.75$ (Figure 17(a)). Three "flip-flop" events take place in the years 2000, 2005, and 2010. The minima first shift close to the horizontal line $\phi_{orb} = 0.25$ after the year 2000, and then to the horizontal line $\phi_{orb} = 0.75$ after the year 2010. Too few $A_{CPS,min,1}$ are available to confirm the $P_{cyc} = 11.0$ years lap cycle (Figures 17(b)–(d)). Although this P_{cyc} value is not very accurate (Table 3), some regularity is present in $A_{orb,binned}$ and $S_{orb,binned}$ changes (Figures 17(f)–(g)).

5.4. Active Longitudes and Amplitudes of V711 Tau

The P_{cyc} lap cycle of V711 Tau is very short—only 150 days. The predicted migration is so fast that the dashed and continuous lines used for illustrating it would totally cover Figure 18(a), and we therefore show this migration only for the first four lap cycles. The $t_{CPS,min,1}$ epochs show a clear tendency to concentrate at phases $\phi_{orb} \approx 0.25$ and 0.75. We can confirm this expected regularity, because the orbital period is very accurate and the t_0 epoch of Equation (1) was determined very recently (Table 1). The $A_{cyc,binned}$ and $S_{cyc,binned}$ changes follow the ϕ_{cyc} phases. The connection of $A_{orb,binned}$ and $S_{orb,binned}$ to the ϕ_{orb} phases is also excellent.

5.5. Active Longitudes and Amplitudes of EI Eri

The number of $t_{CPS,min,1}$ and $A_{CPS,min,1}$ estimates available for EI Eri is only $n = 24$. The migration lines in Figure 19(a) are very steep, because the P_{cyc} lap cycle is only 526 days long. Most of the phases of $t_{CPS,min,1}$ are close to $\phi_{orb} = 0.25$ and 0.75. Again, we succeed in confirming this expected result, because the P_{orb} and t_0 values are reliable (Table 1). The six $A_{cyc,binned}$, $S_{cyc,binned}$, $A_{orb,binned}$, or $S_{orb,binned}$ estimates cannot be used to tell very much about the connection to ϕ_{cyc} or ϕ_{orb}.

5.6. Active Longitudes and Amplitudes of V1149 Ori

The migration of the phases of $t_{CPS,min,1}$ is very stable for V1149 Ori (Figure 20(a)). Three "flip-flop" events occur in the years 1990, 1993, and 2000 when the continuous or dashed migration line crosses the orbital phase $\phi_{orb} = 0.25$. Otherwise, the phases of $t_{CPS,min,1}$ follow the tilted continuous and dashed active longitude migration lines. Even the connection of *individual* A_{CPS} estimates to ϕ_{cyc} or ϕ_{orb} is regular. The $A_{cyc,binned}$ and $S_{cyc,binned}$ changes follow ϕ_{cyc}, and those of $A_{orb,binned}$ and $S_{orb,binned}$ follow ϕ_{orb}.

5.7. Active Longitudes and Amplitudes of σ Gem

How about our favorite star, σ Gem (Jetsu 1996, "Behaves well")? Migration has remained regular (Figure 21(a)). Nearly all minima stayed at $\phi_{orb} = 0.25$ before the year 1992, and then they began to migrate downward. This migration still continues. Four "flip-flop" events occur in the years 1996, 2001, 2005, and 2010. In σ Gem, the minima either concentrate close to horizontal $\phi_{orb} = 0.25$ or 0.75 lines, or they follow the tilted active longitude migration lines. The "flip-flop" events tend to begin and end at phases $\phi_{orb} = 0.25$ and 0.75. All these regularities can be confirmed, because the P_{orb} and t_0 values of σ Gem are reliable. The changes of individual A_{CPS} follow ϕ_{cyc} (Figure 21(b)). Both $A_{cyc,binned}$ and $S_{cyc,binned}$ follow ϕ_{cyc} beyond all expectations (Figures 21(c) and (d)). Individual A_{CPS} estimates also follow ϕ_{orb}, and the largest scatter coincides with $\phi_{orb} = 0.25$ (Figure 21(e)). Changes of $A_{orb,binned}$ and $S_{orb,binned}$ follow ϕ_{orb}.

5.8. Active Longitudes and Amplitudes of FG UMa

After the "flip-flop" event in the year 1993, the migration of FG UMa is regular between the years 1994 and 2001. After the year 2002, the minima show a tendency to concentrate on phases $\phi_{orb} = 0.25$ and 0.75, where numerous "flip-flop" events begin and end (Figure 22(a)). The connection of individual A_{CPS} estimates to ϕ_{cyc} is clear, as well as that of $A_{cyc,binned}$ and $S_{cyc,binned}$ (Figures 22(b), (c), and (d)). The largest of A_{CPS} scatter coincides with $\phi_{orb} = 0.25$ (Figure 22(e)). The $A_{orb,binned}$ and $S_{orb,binned}$ changes are connected to ϕ_{orb} (Figures 22(f) and (g)).

5.9. Active Longitudes and Amplitudes of HU Vir

The light curve minima of HU Vir follow the active longitude continuous migration line between the years 1999 and 2002, except for one "flip-flop" event in the year 1994 (Figure 23(a)). Most of these minima remain at $\phi_{orb} = 0.25$ after the year 2003. Changes of individual A_{CPS} estimates, as well as those of$A_{cyc,binned}$ and $S_{cyc,binned}$, are regular (Figures 23 (b), (c), and (d)). The scatter of A_{CPS} is largest at $\phi_{orb} = 0.25$ (Figure 23(e)). The connection of $A_{orb,binned}$ and $S_{orb,binned}$ to ϕ_{orb} is clear (Figures 23(f) and (g)).

5.10. Active Longitudes and Amplitudes of BM CVn

The minima of BM CVn migrate quite regularly along the tilted continuous active longitude line (Figure 24(a)). However, "flip-flop" events between the continuous and dashed active longitude migration lines take place (e.g., in the years 1996, 2003, and 2016). The minima also show a weak tendency to concentrate on phases $\phi_{orb} = 0.25$ and 0.75, after the year 2007. However, these $\phi_{orb} = 0.25$ and 0.75 levels are uncertain, because P_{orb} of BM CVn is not very accurate (Table 1). The changes of individual A_{CPS} estimates display some regularity (Figure 24(b)). The connection of $A_{cyc,binned}$ and $S_{cyc,binned}$ to ϕ_{cyc} is clear (Figures 24(c) and (d)). The largest scatter of A_{CPS} coincides with $\phi_{orb} = 0.90$ (Figure 24(e)). The $A_{orb,binned}$ and $S_{orb,binned}$ changes follow ϕ_{orb} (Figures 24(f) and (g)).

5.11. Active Longitudes and Amplitudes of V1762 Cyg

The P_{orb} value of V1762 Cyg is accurate, but zero epoch t_0 is far back in time (Table 1). Therefore the $\phi_{orb} = 0.25$ and 0.75 levels in Figure 25 (horizontal dotted lines) are uncertain. The light curve primary minima follow the tilted active longitude lines, especilly the dashed $\phi_{act} = 0.50$ line. There are "flip-flop" events (e.g., in the year 2011 when the dashed migration line crosses the orbital phase $\phi_{orb} = 0.25$; Figure 25(a)). Individual A_{CPS} change regularly (Figure 25(b)). The $A_{cyc,binned}$ and $S_{cyc,binned}$ changes follow ϕ_{cyc} (Figures 25(c) and (d)). The scatter A_{CPS} is largest at $\phi_{orb} = 0.75$ (Figure 25(e)). The $A_{orb,binned}$ and $S_{orb,binned}$ changes are also regular (Figures 25(f) and (g)).

5.12. Active Longitudes and Amplitudes of HK Lac

The t_0 for orbital phases of HK Lac is fixed to an epoch long before our photometry was made (Table 1; i.e., the $\phi_{orb} = 0.25$ and 0.75 levels are uncertain). The lap cycle period is long, $P_{cyc} = 57.5$ years, but it is not accurate (Table 3). The changes of the light curve minima of HK Lac are exceptional (Figure 26(a)). The migration of $t_{CPS,min,1}$ follows the continuous active longitude line between the years 1988 and 2004. Then the slope of linear migration changes, and this slope remains unchanged. One "flip-flop" occurs in the year 2007. The long lap cycle period of HK Lac is the reason for the ϕ_{cyc} gap with no A_{CPS}, $A_{cyc,binned}$, and $S_{cyc,binned}$ estimates in Figures 26(b), (c), and (d). The largest scatter of A_{CPS} occurs close to $\phi_{orb} \approx 0.1$ (Figure 26(e)). The changes of $A_{orb,binned}$ and $S_{orb,binned}$ are regular (Figures 25(f) and (g)).

5.13. Active Longitudes and Amplitudes of II Peg

II Peg is another famous "flip-flop" star (Berdyugina & Tuominen 1998). Our analysis does not reveal a single clear case of "flip-flop" in this CABS (Figure 27(a)). The orbital phases of II Peg are accurate (Table 1; P_{orb} accurate, t_0 recent). The $t_{CPS,min,1}$ phases remained fixed at $\phi_{orb} = 0.25$ between the years 1988 and 1997. Then an extremely regular linear active longitude migration began, and this migration has continued since then (Figure 27(a), tilted dashed line). This reveals how subjective the identification of "flip-flop" events can be (e.g., Berdyugina & Tuominen 1998, their Figure 1). The changes of

individual A_{CPS} estimates are not very regular (Figure 27(b)), while those of $A_{cyc,binned}$ and $S_{cyc,binned}$ certainly are (Figures 27 (c) and (d)). The largest scatter of A_{CPS} coincides with $\phi_{orb} = 0.75$ (Figures 27(e) and (g)). The changes of $A_{orb,binned}$ and $S_{orb,binned}$ are regular (Figures 27(f) and (g)).

6. Discussion

Here we show that a stationary part of the light curve explains MLC similarities and differences of our 14 CABS (Section 6.1), while a nonstationary part of the light curve explains the active longitudes (Section 6.2).

6.1. Stationary Part

Let us assume that the rotation of component A is synchronized with its orbital motion around component B. In this case, component A always turns the same side toward component B, like the Moon always turns the same side toward the Earth.

In the first mode, there is only one spot S1 on A. The brighter side of A is always turned toward B. We observe the maximum projected area of S1 when the line connecting A and B is parallel to our line of sight at epoch Aa. Our notation for this first mode is S1f in Figure 28 (the highest line). MLC minimum coincides with Aa epoch in S1f.

In the second mode, there is again only one spot S1 on A, but the brighter side of A is always turned away from B. The projected area of S1 toward us is largest when the line connecting A and B is parallel to our line of sight at Ac epoch. We denote this second mode as S1b in Figure 28 (the second highest line). MLC primary minimum coincides with Ac epoch in S1b mode.

There is one larger spot S1 and one smaller spot S2 on A in the third mode. S1 is always turned away from B, and S2 is always turned toward B. We observe the maximum projection of S1 when the line connecting A and B is parallel to our line of sight at epoch Aa. Our notation for this third mode is S12fb in Figure 28 (the third highest line). MLC primary minimum coincides with Aa epoch and MLC secondary minimum, with Ac in this S12fb mode.

In the last fourth mode, the roles of S1 and S2 spots are reversed, if compared with the third mode (i.e., both spots have shifted by 180°). S1 is always turned toward B and S1, always away from B. We see the largest projected area of S1 at epoch Ac when S2 is out of sight. Our notation for this fourth mode is S12bf in Figure 28 (the second lowest line). MLC primary and secondary minima coincide with Ac and Aa in this S12bf mode.

The lowest line of Figure 28 shows how ellipticity causes two identical MLC minima at Aa and Ac.

The direction of orbital motion is fixed from left (Aa) to right (Ab) in Figure 28. The results would be the same, if this direction were from right to left, because all e values of our CABS are zero, or close to zero (Table 1).

A comparison between the MLC in "c" panels of Figures 1–14, and the qualitative MLC and the qualitative radial velocity curves on fifth row of Figure 28, reveals the modes of our 14 CABS: 5 in S1f mode (DM UMa, XX Tri, V1149 Ori, BM CVn, HK Lac), 2 in S1b mode (EL Eri, II Peg), 2 in S12fb mode (EI Eri, V478 Lyr), and 5 in S12bf mode (V711 Tau, σ Gem, FG UMa, HU Vir, V1762 Cyg).

The evidence for this "stationary flip-flop" model is overwhelming, as explained in the arguments that follow.

6.1.1. Argument 1: Orbital Motion Connection

MLC of all data show the orbital phases *where* spots concentrate. MLC of two separate samples of data, like those of the first and second part, reveal *where* the largest spot distribution changes take place. The "stationary flip-flop" model explains MLC of all fourteen CABS, especially the connection between orbital phases and MLC primary and secondary minima.

6.1.2. Argument 2: Mean and Amplitude Connection

MLC amplitude decreases when mean brightness increases (e.g., Figure 2), and it increases when mean brightness decreases (e.g., Figure 9). Only dark starspots can cause this effect. The longitudinally evenly distributed spots cancel out in MLC, but longitudinally concentrated spots do not. MLC reveals this mean and amplitude connection, which fits to the "stationary flip-flop" model. For example, Figure 2 indicates that one side of XX Tri is filled with spots that eventually disappear at the brightness maximum, having a low amplitude MLC.

6.1.3. Argument 3: Single and Double Peaked MLC Connection

Low and high MLC amplitudes are possible in S1f and S1b modes. However, S12fb and S12bf modes can have only a low amplitude MLC, because the effects of S1 and S2 spots cancel out. This is the reason why clearly double peaked MLCs have only low A_{All} values (Figures 4, 5, 7, 8, 11, and 12).

6.1.4. Argument 4: Ellipticity Connection

The effects of ellipticity can be understood in the context of the "stationary flip-flop" model (Figure 28, lowest line). Ellipticity can not cause two unequal MLC minima, while spots can. Ellipticity amplifies MLC of S12fb and S12bf modes, but it distorts MLC minima and maxima in S1f and S2b modes, as well as MLC shape. Ellipticity can weaken or strengthen MLC, even in the same object if its modes change. For example, the aforementioned MLC dips of XX Tri (Figure 2(g), $\phi_{orb} \approx 0.25$ and 0.75) and V1149 Ori (Figures 6 (e) and (g), $\phi_{orb} \approx 0.75$) may be an ellipticity effect. In both cases, nearly all spots have faded away, and they do not mask the ellipticity effect.

6.1.5. Argument 5: Flip-flop Connection

The four types of "flip-flop" mode changes are

Type I: S1f ↔ S1b
Type II: S12fb ↔ S12bf
Type III: S1f ↔ S12bf
Type IV: S1b ↔ S12fb.

The modes may also follow this order

S1f ↔ S12fb ↔ S12bf ↔ S1b.

For example, MLC of EI Eri, V478 Lyr, and V1762 Cyg show a Type II "flip-flop" (Figures 5(e) and (g), 11(e) and (g), and 12(e) and (g)).

6.1.6. Some Additional Arguments

All starspots of CABS are not circular, like in our "stationary flip-flop" model of Figure 28. They are not concentrated only on two active longitudes. There are numerous other geometrical and physical phenomena that can induce significant deviations from our simple model. However, considering all these uncertainties, the "stationary flip-flop" model works surprisingly well in all Figures 1–14.

The "flip-flop" phenomenon was originally reported in the single G4 giant FK Com (Jetsu et al. 1993). No unique period, like the orbital period of CABS, can be used to compute MLC for single giants like FK Com, or for single main sequence stars like LQ Hya (Lehtinen et al. 2012, K1 V). One solution might be to compute MLC for tested periods within a short interval at both sides of the active longitude period. The tested period with the highest MLC amplitude might reveal similar results as we report here.

All our MLCs are not necessarily representative samples, because we have not observed the full spot cycles of all CABS (e.g., Figure 2(a), XX Tri). It may also be that the "flip-flop" events are connected to spot cycles (e.g., Berdyugina 2005). A sliding window MLC within a time interval shorter than ΔT may reveal such regularities.

Finally, we return back to σ Gem, because the discovery of its ellipticity (Roettenbacher et al. 2015) motivated the current study. This star is a special case, where S1 and S2 nearly equally strong, and even small changes in spot areas can trigger "flip-flop" events "aided" by the ellipticity effect.

6.2. Nonstationary Part

The model for the binned MLC data (Equation (2)) is stationary, because the active longitudes are locked to the synchronized orbital motion and rotation frame with the period $P_{\rm orb}$. This model does not explain the regular migration of light curve minima (Figures 15–27, "a" panels). Such migration has already been reported in binaries and single stars—for example, by Henry et al. (1995a, four CABS), Hackman et al. (2011, II Peg), Kajatkari et al. (2014, σ Gem), or Hackman et al. (2013, FK Com). Our results in Figures 15–27 show that the CABS light curves contain a nonstationary part

$$f_1(t,\bar{\beta}_1) = M_1 + \sum_{k=1}^{K_1} A_k \cos\left(\frac{2\pi k t}{P_{\rm act}}\right) + B_k \sin\left(\frac{2\pi k t}{P_{\rm act}}\right), \quad (7)$$

where $\bar{\beta}_1 = [M_1, A_1, ..., A_{K_1}, B_1, ..., B_{K_1}]$ are the free parameters and $K_1 = 1$ is probably sufficient, because the $t_{\rm CPS,min,1}$ changes have a linear connection to $\phi_{\rm orb}$ (Figures 15–27, panels "a"). This is the dark longitudinally dominating nonstationary spot S3 that rotates once around the surface of component A during every $P_{\rm cyc}$ lap cycle (see Figure 29, dark vertical line). We use a vertical line to denote the longitude of this spot S3, because our figure is already quite crowded by spots S1 and S2. If $f_1(t,\bar{\beta}_1)$ is double peaked, then another nonstationary spot S4 rotates with the period $P_{\rm act}$. For obvious reasons, we have not tried to squeeze spot S4 into Figure 29. We compute the phases $\phi_{\rm act}$ of this nonstationary part $f_1(\phi_{\rm act})$ from the active longitude ephemeris of Equation (5).

MLC represent the second stationary part,

$$f_2(t,\bar{\beta}_2) = M_2 + \sum_{k=1}^{K_2} C_k \cos\left(\frac{2\pi k t}{P_{\rm orb}}\right) + D_k \sin\left(\frac{2\pi k t}{P_{\rm orb}}\right), \quad (8)$$

where $\bar{\beta}_2 = [M_2, C_1, ..., C_{K_2}, D_1, ..., D_{K_2}]$ are the free parameters, and $K_2 = 1$ or 2. We compute the phases $\phi_{\rm orb}$ of this stationary part $f_2(\phi_{\rm orb})$ from the orbital period zero epoch (Table 2, Ab epoch in Equation (1)).

Hence the suitable CABS light curve model is

$$f(t,\bar{\beta}) = f_1(t,\bar{\beta}_1) + f_2(t,\bar{\beta}_2), \quad (9)$$

where the free parameters M_1 and M_2 are combined to into one free parameter $M = M_1 + M_2$. Note that the sketches in Figures 28 and 29 are valid only for CABS that are not eclipsing binaries, and this model cannot therefore be applied to the light curves of eclipsing binaries. We also assume that the variations are caused by dark starspots.

This model is linear. The nonstationary $f_1(t,\bar{\beta}_1)$ and stationary $f_2(t,\bar{\beta}_2)$ parts have a unique solution. The interference between these two waves is impossible to foresee without numerical modeling. We will show how the model of Equation (9) explains the four "flip–flop" types of Section 6.1.5.

There are striking similarities in Figures 15–27. The amplitude changes follow both $P_{\rm cyc}$ and $P_{\rm orb}$. This reflects the interference of two "waves" (Equations (7) and (8)). The "flip-flop" events tend to occur when the active longitudes migrate through phases $\phi_{\rm orb} = 0.25$ and 0.75. The relative strengths of the amplitudes of the stationary part $f_2(t,\bar{\beta}_2)$ and the nonstationary part $f_1(t,\bar{\beta}_1)$ can be reversed at these particular phases. This phenomenon is illustrated in the cases when the minima first follow the horizontal dotted lines and then begin to follow the the tilted continuous or dashed lines, or vice versa (Figures 15–27, "a" panels). The two waves can either amplify each other or cancel out at these same phases $\phi_{\rm orb} = 0.25$ and 0.75. Hence there are numerous reasons for the large scatter of the amplitude values at these two phases. All these regularities allow us to identify the "flip-flop" events nearly unambiguously.

The sketches in Figure 29 illustrate one $P_{\rm cyc}$ lap cycle. This model works like giant clock, where the nonstationary wave rotates once around component A during every lap cycle. The locations of spots S1 and S2 are stable in the synchronized orbital and rotational frame. The sizes and/or temperatures of these spots may change. The dramatic events, like "flip-flop" phenomena, are more frequent when spot S3 crosses the longitudes of S1 and S2.

If the unseen secondary component B has spots, its stationary spot configuration most probably resembles that of component A (i.e., the stationary spots of component B also reside at the longitudes coinciding with the line connecting the centers of components A and B). If this B secondary is a white dwarf, our model predicts its location with respect to spots S1 an S2 on component A. It may now be easier to combine light curves to surface imaging maps (e.g., Hackman et al. 2011; Lindborg et al. 2013), because our model gives the longitudes of spots S1, S2, S3, and S4 at any given epoch in time.

The results for XX Tri reveal that the free parameters of this model of Equation (9) depend on time (e.g., the mean level of brightness $M = M(t)$). The cycle for the mean of XX Tri (see Figure 2(a)) is clearly much longer than the $P_{\rm cyc} = 7.8$ years lap cycle in the light curve amplitude (Table 3). This problem of temporally changing free parameters can be solved by modeling the light curves of Equation (9) during time intervals (i.e., windows) shorter than the whole time span of the data

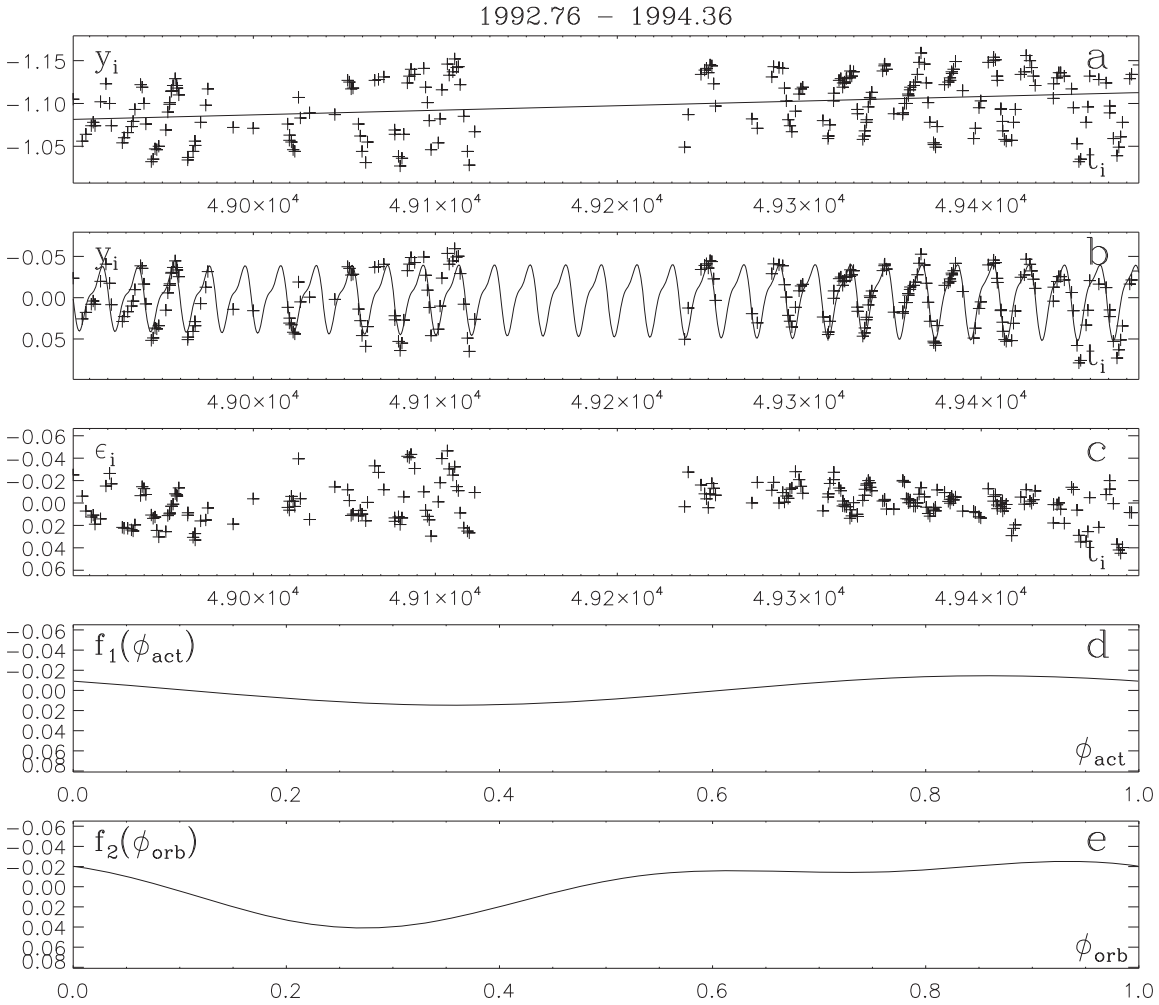

Figure 30. Arbitrary slice of σ Gem photometry. (a) Original photometry and a linear fit (solid line). (b) Original photometry minus linear fit, and model of Equation (9) ($K_1 = 1$, $K_2 = 2$, $M = M_1 = M_2 = 0$). (c) Model residuals ϵ_i. (d) Nonstationary part $f_1(\phi_{act})$. (e) Stationary part $f_2(\phi_{orb})$.

(ΔT), like with the CPS method (Lehtinen et al. 2011). The information of the long-term evolution of the magnetic fields of CABS is probably coded into the free parameters of this model. One advantage of our model is that the stationary and nonstationary parts of this magnetic field can be uniquely separated and solved from the light curves.

Here is our short analysis recipe for CABS light curves. *Solve the active longitude period P_{act} from the epochs of minimum ($t_{CPS,min,1}$). Use the known orbital period (P_{orb}), and apply the model (Equation (9)) to the original photometry.*

We show two arbitrary slices of σ Gem photometry in Figure 30 ($\Delta T = 589$ days) and Figure 31 ($\Delta T = 230$ days). The nonstationary and stationary orders of the model for the first slice are $K_1 = 1$ and $K_2 = 2$ (Figure 30). Note that our model gives a unique solution also within gaps of data. Subtraction of the same linear trend from the data at both sides of the gap does not fully eliminate the mean level changes (Figures 30(a) and (b)), and the mean residuals are therefore quite large $0\overset{m}{.}012$ (Figure 30(c)). The two models in Figure 31(b) have $K_1 = 1$ and $K_2 = 2$ (continuous line), and $K_1 = 2$ and $K_2 = 2$ (dashed line). Their mean residuals are $0\overset{m}{.}007$ (Figure 31(c), crosses) and $0\overset{m}{.}006$ (Figure 31(c), diamonds). These values are comparable to the accuracy of our data, $0\overset{m}{.}006$. Comparison of Figures 30(d) and (e) and 31(d) and (e) shows that the nonstationary part, $f_1(\phi_{act})$, and stationary part, $f_2(\phi_{orb})$, of this CABS are indeed changing. The residuals of our model indicate that if the drift of short-lived spots is present in σ Gem, this effect is weak. Although the presence of surface differential rotation is not observed in the movement of starspots of σ Gem, this does not prove that surface differential rotation is absent. However, the stationary and nonstationary spots in σ Gem seem to defy differential rotation.

We give a slightly different recipe for single stars, because they have no P_{orb} value. *Solve the active longitude period P_{act} from the minima epochs ($t_{CPS,min,1}$). Rename P_{orb} to P_{single} in Equation (8). Test a period interval ±15% at both sides of P_{act} (i.e., the tested period interval is $P_{min} = 0.85P_{act}$ and $P_{max} = 1.15P_{act}$).* A suitable step for the tested frequencies is $f_{test} = 1/(\Delta T \times \mathrm{OFAC})$, where ΔT is the time span of the data and a suitable value for the overfilling factor is OFAC = 10. The tested frequencies f_{test} are all integer multiples of f_{step} between $f_{min} = 1/P_{max}$ and $f_{max} = 1/P_{min}$. Fit our linear model (Equation (9)) to the original photometry using $P_{single} = 1/f_{test}$. Find the f_{test} value that gives the best fit to the data, $f_{test,best}$. It gives the rotation period, $P_{single} = 1/f_{test,best}$, of this single star. A suitable test statistic is $z_{test} = \sqrt{(1/n)\sum_{i=1}^{n}\epsilon_i^2}$, where ϵ_i are the residuals of the model of Equation (9), with the known P_{act} value and the tested P_{single} value. This z_{test} is approximately the mean of $|\epsilon_i|$ of each tested model.

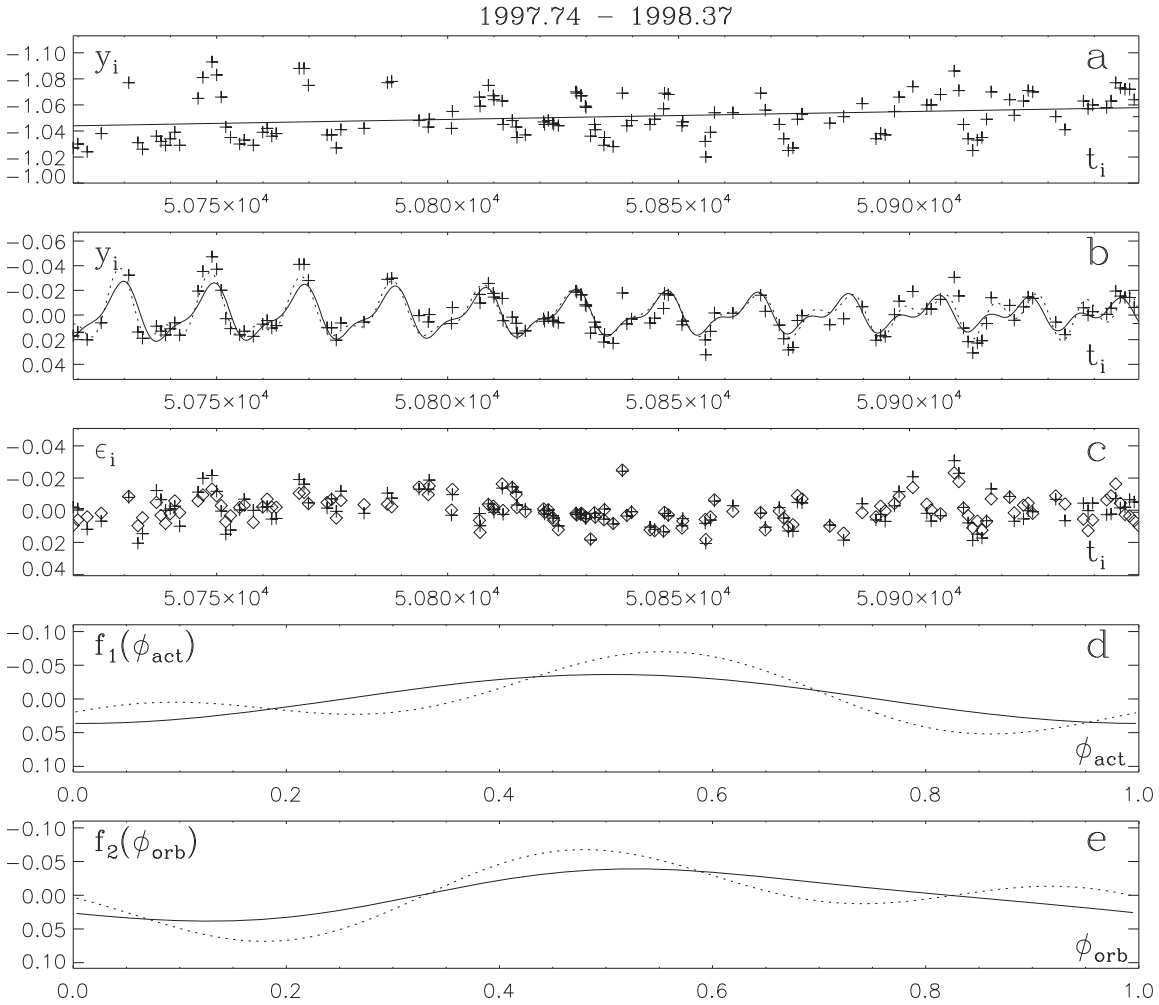

Figure 31. Another slice of σ Gem photometry. (a) Original photometry and a linear fit (solid line). (b) Original photometry minus linear fit first model (Equation (9); $K_1 = 1$, $K_2 = 2$, $M = M_1 = M_2 = 0$, continuous line) and second model (Equation (9); $K_1 = 2$, $K_2 = 2$, $M = M_1 = M_2 = 0$, dashed line). (c) Residuals of first model (crosses) and second model (diamonds). (d) Nonstationary part $f_1(\phi_{act})$ of the first and second model (continuous and dashed lines). (e) Stationary part $f_2(\phi_{orb})$ of the first and second model (continuous and dashed lines).

We tested this method on the single star FK Com using $P_{act} = 2.401151$ days to a short slice of photometry from Hackman et al. (2013; $\Delta T = 126$ days). A linear fit to these data is shown in Figure 32(a). This linear trend was removed from the data before computing the z_{test} periodograms. We show the periodograms for two models (Equation (9), $K_1 = 1$, $K_2 = 2$) and (Equation (9), $K_1 = 2$, $K_2 = 2$) in Figure 32(b). The best value was $P_{single} = 2.3935$ days. The two solutions for the light curve of FK Com overlap in Figure 32(c), because their maximum difference is $0\overset{m}{.}006$. The mean residuals of these models are $0\overset{m}{.}009$ and $0\overset{m}{.}008$. The P_{act} period of FK Com was determined from the light curve minima, like in our CABS analysis. Hence it represents the nonstationary spot S3 detached from the P_{single} rotation frame of FK Com. Refinement of P_{act} can *only* be achieved from an analysis of new $t_{CPS,min,1}$ data. Our $P_{single} = 2.3935$ days value represents the stationary part attached to the rotation frame of FK Com. The accuracy of this value could be determined, for example, with the bootstrap method (see Jetsu & Pelt 1999, Section 4). However, this value is certainly not final, because different slices of photometry from Hackman et al. (2013) gave different values. A lot of data must be analyzed using a much more careful subtraction of the changes of the mean level. This type of an analysis is made to the photometry of numerous data slices of FK Com photometry by Jetsu (2016, Table 3), where the P_{single} value converges to an extremely accurate final value, just like the orbital periods P_{orb} of binary stars (or the rotation periods of other single stars). Such a result is self-evident, because both components of all our CABS have $P_{orb} = P_{single}$. When the two stars in FK Com coalesced, their P_{orb} became P_{single}, or equivalently P_{orb} became meaningless. We emphasize that the P_{act} value of FK Com is already known, but more work is required to determine its P_{single} value. This is one of the advantages of our model: the rotation periods of single active stars are no longer based on the observed changing P_{phot} values (Figure 32(b), only one clear minimum).

Now we turn to the light curve predictability with Equation (9), for CABS and single active stars. It is at least partly possible to predict the observed light curves changes when the P_{orb} or P_{single} and P_{act} values are known. The light curve minima follow the "lattice" $\phi_{orb} = \phi_{single} = 0.25$ or 0.75, and $\phi_{act} = 0.00$ or 0.5 (Figures 15–27, "a"panels). The difference $\Delta P_{orb/single-act} = |P_{orb} - P_{act}| = |P_{single} - P_{act}|$ determines the scale of observed light curve period changes. If the nonstationary part $f_1(t, \bar{\beta}_1)$ is weak, then P_{act} is absent and the observed light curve period is close to P_{orb}. The opposite is true

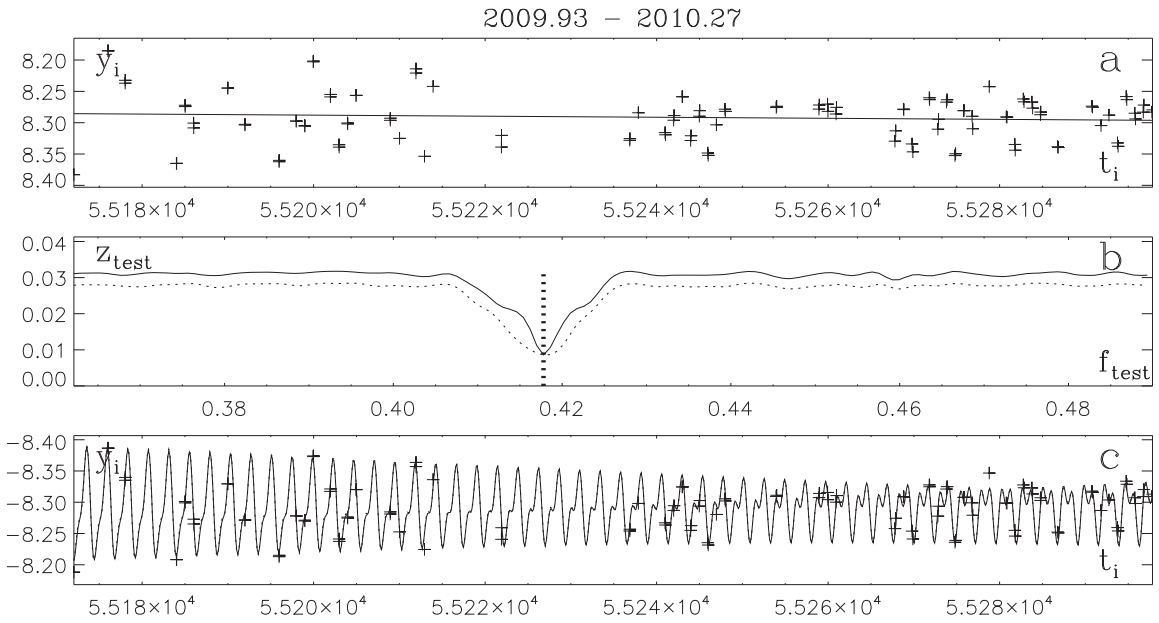

Figure 32. Slice of FK Com photometry. (a) Original photometry and a linear fit (solid line). (b) $z_{test}(f_{test})$ periodograms for the first model (Equation (9), $K_1 = 1$, $K_2 = 2$, $M = M_1 = M_2 = 0$, $P_{act} = 2.401151$ days, continuous line) and second model (Equation (9), $K_1 = 2$, $K_2 = 2$, $M = M_1 = M_2 = 0$, $P_{act} = 2.401151$, dashed line) and best period $P_{single} = 2.3935$ days (vertical thick dashed line). The tested frequency interval is $f_{min} = 1/P_{max}$ and $f_{max} = 1/P_{min}$, where $P_{min} = 0.85P_{act}$ and $P_{max} = 1.15P_{act}$. (c) Respective light curves of the previous two models with $P_{single} = 2.3935$, continuous and dashed line. Note that the difference between these two models is so small that the two different lines cannot be resolved.

when $f_2(t, \bar{\beta}_1)$ is weak. If $\Delta P_{orb/single-act}$ is small, the observed light curve period changes are small, and vice versa. The observed period changes reflect this difference $\Delta P_{orb/single-act}$ between two constant periods (i.e., not surface differential rotation). One period may dominate over the other one for a long period of time (e.g., in II Peg the stationary P_{orb} dominated between the years 1987 and 1995), and then the nonstationary P_{act} began to dominate, and this domination has continued to the year 2015 (Figure 27(a)). The case of HK Lac is very similar (Figure 26(a)). The $f_1(t, \bar{\beta}_1)$ and $f_2(t, \bar{\beta}_2)$ amplitudes determine the maximum scale for the observed light curve amplitudes. For example, perhaps the observed surface differential rotation in the light curves of slowly rotating stars is not larger, but the ratio $\Delta P_{orb/single\text{-}act}/P_{orb}$ probably is. As for another example, if no active longitude is discovered, then only the nonstationary part is present. No switches between the domination of $f_1(t, \bar{\beta}_1)$ and $f_2(t, \bar{\beta}_2)$ can occur. This reduces the observed period variations (e.g., in the Sun and other inactive stars). The results in Lehtinen et al. (2016) indicate that the nonstationary part is absent in young inactive solar-type stars, because no active longitudes (P_{act}) are detected.

The periods P_{orb} and P_{act} of these CABS are constant for long periods of time. The observed photometric periods of these stars appear to change, but this is probably caused by the interference of two constant period waves. Does this then mean that there is no surface differential rotation in these CABS? It has been known for a long time that surface differential rotation in these rapidly rotating stars is weak (e.g., Hall 1991), but no one has ever seriously claimed that surface differential rotation is totally absent. Surface differential rotation may be present in these CABS, but the locations of stationary S1 and S2 spots seem stable, as well the movement of the nonstationary spots S3 and S4. Could the driving mechanism of magnetic fields in these CABS be the rotation of plasma of free charged particles producing stationary and nonstationary magnetic field waves? Spots S1–S4 are simply the signatures of these waves. And where there is a wave, and another wave, there are probably numerous waves. We have discovered only the two strongest waves in these CABS. Could the interference of stationary and nonstationary waves sustain long-lived magnetic fields? If these waves are stronger in rapidly rotating stars late type stars, their interference produces stronger spots. Could interference explain the differences between the magnetic fields of early and late type stars? In early type stars, their radiative envelopes allow the waves of the magnetic field to remain stable. In late type stars, convection complicates things. Thus quasiperiodic spot distribution changes are observed in late-type stars, and stable spot distributions are observed in early type stars. A more sophisticated version of our model could be a sum of spherical functions describing the stationary and nonstationary magnetic field waves. Perhaps the free parameters of this model could be solved from observations.

This brings us back to the two currently known alternatives for magnetic fields in all spectral types:

1. Rotation and convection (dynamo).
2. Fossil fields.

We admittedly only speculate about a third alternative:

3. Rotation and interference.

.

"Rotation" is present only in two of these three alternatives. Or is "rotation" present in all three alternatives? Our expertise lies in time series analysis, not in the modeling stellar magnetic fields. Therefore this interference hypothesis of ours is tentative.

Here is our simple analogy. The orbital and rotation periods of the Moon are equal. Due to this synchronization, we never see the far side of Moon when it is illuminated by the Sun. Imagine that a giant large dark circular screen would begin to rotate around the Moon with a period of, for example, 10 years (P_{act}). This is what we see in CABS and single stars. The main

differences are that the rotation period of Earth is not synchronized with the orbital motion of the Moon, and the "spot" on the Moon is not stuck to its surface, but moves due to the illumination of the Sun.

7. Conclusions

We compute MLC of 14 CABS as functions of orbital phase $\phi_{\rm orb}$. The phase $\phi_{\rm orb} = 0$ is fixed to the epoch of radial velocity maximum. The phases of MLC minima concentrate on $\phi_{\rm orb} = 0.25$ and/or 0.75, and reveal the presence of a long-lived concentrated starspot distribution. The line connecting the centers of A and B components intersects the longitudes of this stationary part of starspot distribution. This part can be present on *only one* of these longitudes (Section 6.1; S1f and S1b modes), or on *both* of these longitudes (Section 6.1; S12fb and S12bf modes). We discuss the different types of "flip-flop" events between these modes, and also show that such events occur in our data (Section 6.1.5). These modes are also stationary in the rotational frame of reference, because the orbital motion and rotation of these CABS is synchronized, $P_{\rm orb} = P_{\rm rot}$. We denote the light curve of this stationary part as $f_2(\phi_{\rm orb})$ (Equations (1) and (8)).

Another long-lived part of starspot distribution, concentrating on the active longitudes, is discovered from the primary minima $t_{\rm CPS,min,1}$ of the short-term seasonal light curves. These active longitudes are non-stationary in the rotational frame of reference, because their rotation period $P_{\rm act}$ is not equal to $P_{\rm orb} = P_{\rm rot}$. Our notation for the light curve of this non-stationary part is $f_1(\phi_{\rm act})$ (Equations (5) and (7)). This migrating non-stationary part (i.e., the active longitudes) crosses the longitudes of the stationary part when the $t_{\rm CPS,min,1}$ epoch phases computed from Equation (1) fulfil $\phi_{\rm orb} = 0.25$ and/or 0.75. The interference of $f_1(\phi_{\rm act})$ and $f_2(\phi_{\rm orb})$ light curves should therefore be strongest at these two orbital phases. If the observed light curves are interference of these two "real" light curves, the scatter of the amplitudes $A_{\rm CPS}$ of the observed light curves is largest at $\phi_{\rm orb} = 0.25$ and/or 0.75. If this interference is a real phenomenon, the observed light curve amplitude $A_{\rm CPS}$ changes should also follow a lap cycle period $P_{\rm cyc}$ (Equation (4)). Both of these effects are present in our data (Figures 15–27).

We combine these two "real" light curves in the model of Equation (9). This model is applied to three slices of real photometric data. The time spans of these slices are $\Delta T = 586$ days (Figure 30, σ Gem), $\Delta T = 230$ days (Figure 31, σ Gem), and $\Delta T = 126$ days (Figure 32, FK Com). The mean residuals of these models are between $0\overset{\rm m}{.}006$ and $0\overset{\rm m}{.}012$. This is an excellent result, considering that the CPS method, or the power spectrum method, can only model data sets having a time span of $\Delta T = 30$ days or less (e.g., Kajatkari et al. 2015). The main advantage of our model of Equation (9) is that it can adjust to changes of the amplitude and the shape of the light curve. Except for the previously mentioned three slices, we do not proceed here to analyse the seasonal real light curves $f_1(\phi_{\rm act})$ and $f_2(\phi_{\rm orb})$ of our 14 CABS. The first such study for any individual star is presented in Jetsu (2016), where the model of Equation (9) is applied to long-term photometry of FK Com. Many results of that study support the idea that the observed light curves of FK Com are interference of the "real" light curves $f_1(\phi_{\rm act})$ and $f_2(\phi_{\rm orb})$.

If $f_1(\phi_{\rm act})$ dominates, the $\phi_{\rm orb}$ phases of $t_{\rm CPS,min,1}$ follow the two *tilted* lines $\phi_{\rm act} = 0.00$ or 0.50 in Figures 15–27(a). If $f_2(\phi_{\rm orb})$ dominates, the $\phi_{\rm orb}$ phases of $t_{\rm CPS,min,1}$ follow the two *horizontal* lines $\phi_{\rm orb} = 0.25$ or 0.75. All the previously mentioned four lines are unambiguous, because the $t_{\rm CPS,min,1}$ epochs are unambiguous in time. The uncertainty in the horizontal $\phi_{\rm orb} = 0.25$ or 0.75 levels depends on the accuracy of $P_{\rm orb}$ and t_0 values in Equation (1). New radial velocity measurements are needed to refine these two values of CABS. It is certain that $P_{\rm orb}$ and t_0 will converge to very accurate final values. The $P_{\rm orb}$ values of CABS are not constant. The typical changes are $\Delta P/P \sim 10^{-5}$ (e.g., Applegate 1992). However, the long-term mean of these alternating $P_{\rm orb}$ changes is much more accurate.

When new more accurate $P_{\rm orb}$ and t_0 values are available, they will not only provide more accurate $\phi_{\rm orb} = 0.25$ or 0.75 levels, or more accurate $P_{\rm cyc}$ values (Equation (4)). Jetsu (1996) has already shown that the $P_{\rm rot}$ value of FK Com converges under the assumption that the known $P_{\rm act}$ value is constant. This period finding test can be modified to a *reversed test* for CABS. Numerous slices of photometry can be used to check if the $P_{\rm act}$ of some CABS converges under the assumption that the known $P_{\rm orb}$ value is constant. At the moment, the $P_{\rm act}$ values of CABS are determined from the $t_{\rm CPS,min,1}$ epochs (e.g., with the Kuiper test). Although the critical levels of many active longitude detections are extreme (e.g., Table 3, $Q_{\rm K} = 2 \times 10^{-11}$ for XX Tri), the analyzed data may have contained $t_{\rm CPS,min,1}$ epochs of light curves where $f_2(\phi_{\rm orb})$ dominates. The $t_{\rm CPS,min,1}$ values of such light curves mislead the Kuiper test analysis. The *reversed test* should not only confirm the earlier active-longitude periods detections, but it probably also converges to a more accurate $P_{\rm act}$ value for every CABS. It is a fact that active longitude periods $P_{\rm act}$ are discovered in CABS, even if $f_2(\phi_{\rm orb})$ determines the $t_{\rm CPS,min,1}$ values of some light curves. This may mean that the $P_{\rm act}$ value of every CABS is constant, and that $P_{\rm act}$ is a permanent fundamental parameter, just like the $P_{\rm orb}$ and $P_{\rm rot}$ parameters. Future photometry and radial velocity measurements can be used to test this idea (i.e., the convergence of the $P_{\rm act}$ parameter of CABS).

Here, we have presented a general model for the light curves of chromospherically active single and binary stars (Equation (9)). This model explains the connection between orbital motion, long-term starspot distribution changes, ellipticity, and "flip-flop" events in CABS. The Ancient Egyptians discovered Algol's regular eclipses. Some day, this model of ours may perhaps be referred to as something discovered by the Ancient Finns and Americans. The history of mankind pales when compared to the millions or billions of years that these CABS have already spent in synchronous orbital motion and rotation. Two stars A and B are endlessly staring at each other's faces. Spots S3 and S4 (if present) occasionally arrive to meet spots S1 and S2 at every multiple epoch of half lap cycle $P_{\rm cyc}$. Except for changes in the spot filling factors and/or temperatures, this peaceful arrangement is nearly eternal. This idea of "nothing ever happens" is something that truly works in astronomical timescales. The geometry of the magnetic fields in these CABS does in some ways begin to resemble the never changing geometry of the magnetic fields of Ap stars, the oblique rotator model (e.g., Jetsu et al. 1992, CQ Uma). Are we observing interference waves of "Oh Be A Fine Girl, Kiss Me Right Now or Soon" (i.e., of both early and late spectral types)?

If the real light curves $f_1(\phi_{act})$ and $f_2(\phi_{orb})$ cancel out each other, we observe a straight line. This light curve mean level provides a measure of the spot area, the filling factor, relative to other previous epochs. Otherwise, it seems like nothing happens, whatever the amplitudes of the real light curves may be. In this case, we cannot solve the real $f_1(\phi_{act})$ and $f_2(\phi_{orb})$ curves from the observations. However, let us assume that we have observations also before and/or after the time interval that the observed light curve is constant. In this case, it is possible to model this interval of constant brightness, and solve the $f_1(\phi_{act})$ and $f_2(\phi_{orb})$ curves, if the observations are accurate. Could this phenomenon be common in the universe, like the repeating voids and galaxy concentrations? For example, could two "wavefronts" of different forces or energies cancel out in voids, but not in galaxy concentrations? This would not violate the law of conservation of energy, because the currently observed total energy in the universe would remain the same. We dare to express this simple idea, because natural sciences border on, and are based on, the philosophy of science. It took us 70 years to "see behind" the light curves of CABS (Kron 1947), but perhaps this gave us one clue of how to "see behind" empty space (where two or more forces cancel out).

This work has made use of the SIMBAD database at CDS, Strasbourg, France, and NASA's Astrophysics Data System (ADS) services. The automated astronomy program at Tennessee State University has been supported by NASA, NSF, TSU, and the State of Tennessee through the Centers of Excellence program.

References

Applegate, J. H. 1992, ApJ, 385, 621
Balona, L. A. 1987, SAAOC, 11, 1
Barrado y Navascues, D., de Castro, E., Fernandez-Figueroa, M. J., Cornide, M., & Garcia Lopez, R. J. 1998, A&A, 337, 739
Berdyugina, S. V. 2005, LRSP, 2, 8
Berdyugina, S. V., Jankov, S., Ilyin, I., Tuominen, I., & Fekel, F. C. 1998, A&A, 334, 863
Berdyugina, S. V., & Tuominen, I. 1998, A&A, 336, L25
Bopp, B. W., & Dempsey, R. C. 1989, PASP, 101, 516
Bopp, B. W., Fekel, F. C., Aufdenberg, J. P., Dempsey, R., & Dadonas, V. 1993, AJ, 106, 2502
Cardini, D. 2005, A&A, 430, 303
Catalano, S., & Rodonò, M. 1967, MmSAI, 38, 395
Chugainov, P. F. 1966, IBVS, 172, 1
Crampton, D., Dobias, J., & Margon, B. 1979, ApJ, 234, 993
Cutispoto, G. 1993, A&AS, 102, 655
Cutispoto, G. 1995, A&AS, 111, 507
Donati, J.-F., Brown, S. F., Semel, M., et al. 1992, A&A, 265, 682
Drake, A. J., Graham, M. J., Djorgovski, S. G., et al. 2014, ApJS, 213, 9
Duemmler, R., Ilyin, I. V., & Tuominen, I. 1997, A&AS, 123, 209
Eker, Z., Ak, N. F., Bilir, S., et al. 2008, MNRAS, 389, 1722
Fekel, F. C. 1988, AJ, 95, 215
Fekel, F. C., & Henry, G. W. 2005, AJ, 129, 1669
Fekel, F. C., Henry, G. W., Eaton, J. A., Sperauskas, J., & Hall, D. S. 2002, AJ, 124, 1064
Fekel, F. C., Moffett, T. J., & Henry, G. W. 1986, ApJS, 60, 551
Fekel, F. C., Quigley, R., Gillies, K., & Africano, J. L. 1987, AJ, 94, 726
Fekel, F. C., Strassmeier, K. G., Weber, M., & Washuettl, A. 1999, A&AS, 137, 369
Fekel, F. C., Jr. 1983, ApJ, 268, 274
García-Alvarez, D., Foing, B. H., Montes, D., et al. 2003, A&A, 397, 285
Glebocki, R., & Stawikowski, A. 1995, AcA, 45, 725
Gorza, W. L., & Heard, J. F. 1971, PDDO, 3, 99
Griffin, R. F., & Fekel, F. C. 1988, JApA, 9, 213
Hackman, T., Mantere, M. J., Jetsu, L., et al. 2011, AN, 332, 859
Hackman, T., Pelt, J., Mantere, M. J., et al. 2013, A&A, 553, A40
Hall, D. S. 1972, PASP, 84, 323
Hall, D. S. 1991, in IAU Coll. 130, The Sun and Cool Stars. Activity, Magnetism, Dynamos, ed. I. Tuominen, D. Moss, & G. Rüdiger (Berlin: Springer), 353
Hall, D. S., Fekel, F. C., Henry, G. W., & Barksdale, W. S. 1991, AJ, 102, 1808
Hatzes, A. P. 1998, A&A, 330, 541
Henry, G. W., Eaton, J. A., Hamer, J., & Hall, D. S. 1995a, ApJS, 97, 513
Henry, G. W., Fekel, F. C., & Hall, D. S. 1995b, AJ, 110, 2926
Hoffmeister, C. 1965, VeSon, 6, 97
Jetsu, L. 1996, A&A, 314, 153
Jetsu, L. 2016, A&A, submitted (arXiv:1612.08890)
Jetsu, L., Kokko, M., & Tuominen, I. 1992, A&A, 265, 547
Jetsu, L., & Pelt, J. 1996, A&AS, 118, 587
Jetsu, L., & Pelt, J. 1999, A&AS, 139, 629
Jetsu, L., Pelt, J., & Tuominen, I. 1993, A&A, 278, 449
Jetsu, L., & Porceddu, S. 2015, PLoSO, 10, e0144140
Jetsu, L., Porceddu, S., Lyytinen, J., et al. 2013, ApJ, 773, 1
Kajatkari, P., Hackman, T., Jetsu, L., Lehtinen, J., & Henry, G. W. 2014, A&A, 562, A107
Kajatkari, P., Jetsu, L., Cole, E., et al. 2015, A&A, 577, A84
Koen, C., & Eyer, L. 2002, MNRAS, 331, 45
Kron, G. E. 1947, PASP, 59, 261
Lehtinen, J., Jetsu, L., Hackman, T., Kajatkari, P., & Henry, G. W. 2011, A&A, 527, A136
Lehtinen, J., Jetsu, L., Hackman, T., Kajatkari, P., & Henry, G. W. 2012, A&A, 542, A38
Lehtinen, J., Jetsu, L., Hackman, T., Kajatkari, P., & Henry, G. W. 2016, A&A, 588, A38
Lindborg, M., Mantere, M. J., Olspert, N., et al. 2013, A&A, 559, A97
Osten, R. A., & Saar, S. H. 1998, MNRAS, 295, 257
Özeren, F. F., Doyle, J. G., & Jevremovic, D. 1999, A&A, 350, 635
Porceddu, S., Jetsu, L., Markkanen, T., & Toivari-Viitala, J. 2008, Cambridge Archaeol. J., 18, 327
Roettenbacher, R. M., Monnier, J. D., Henry, G. W., et al. 2015, ApJ, 807, 23
Samus, N. N., Durlevich, O. V., & Kazarovets, R. V. 1997, BaltA, 6, 296
Siltala, L., Jetsu, L., Hackman, T., et al. 2016, arXiv:1601.03536
Strassmeier, K. G. 1990, ApJ, 348, 682
Strassmeier, K. G. 1999, A&A, 347, 225
Strassmeier, K. G. 2009, A&ARv, 17, 251
Strassmeier, K. G., Hall, D. S., Eaton, J. A., et al. 1988, A&A, 192, 135
Strassmeier, K. G., & Olah, K. 1992, A&A, 259, 595